



Deep VLA Observations of the Cluster 1RXS J0603.3+4214 in the Frequency Range of 1–2 GHz

K. Rajpurohit¹ , M. Hoeft¹, R. J. van Weeren², L. Rudnick³, H. J. A. Röttgering⁴, W. R. Forman² , M. Brüggen⁵, J. H. Croston⁶ , F. Andrade-Santos² , W. A. Dawson⁷ , H. T. Intema⁴ , R. P. Kraft², C. Jones², and M. James Jee^{8,9}

¹ Thüringer Landessternwarte, Sternwarte 5, D-07778 Tautenburg, Germany; kamlesh@tls-tautenburg.de

² Harvard Smithsonian Center for Astrophysics, 60 Garden Street Cambridge, MA 02138, USA

³ Minnesota Institute for Astrophysics, University of Minnesota, 116 Church Street S.E., Minneapolis, MN 55455, USA

⁴ Leiden Observatory, Leiden University, P.O. Box 9513, NL-2300 RA Leiden, The Netherlands

⁵ Hamburger Sternwarte, Universität Hamburg, Gojenbergsweg 112, D-21029 Hamburg, Germany

⁶ School of Physical Sciences, The Open University, Walton Hall, Milton Keynes, MK6 7AA, UK

⁷ Lawrence Livermore National Lab, 7000 East Avenue, Livermore, CA 94550, USA

⁸ Department of Astronomy and Center for Galaxy Evolution Research, Yonsei University, 50 Yonsei-ro, Seoul 03722, Korea

⁹ Department of Physics, University of California, Davis, One Shields Avenue, Davis, CA 95616, USA

Received 2017 August 22; revised 2017 November 30; accepted 2017 December 1; published 2018 January 8

Abstract

We report L-band VLA observations of 1RXS J0603.3+4214, a cluster that hosts a bright radio relic, known as the Toothbrush, and an elongated giant radio halo. These new observations allow us to study the surface brightness distribution down to 1 arcsec resolution with very high sensitivity. Our images provide an unprecedented detailed view of the Toothbrush, revealing enigmatic filamentary structures. To study the spectral index distribution, we complement our analysis with published LOFAR and GMRT observations. The bright “brush” of the Toothbrush shows a prominent narrow ridge to its north with a sharp outer edge. The spectral index at the ridge is in the range $-0.70 \leq \alpha \leq -0.80$. We suggest that the ridge is caused by projection along the line of sight. With a simple toy model for the smallest region of the ridge, we conclude that the magnetic field is below $5 \mu\text{G}$ and varies significantly across the shock front. Our model indicates that the actual Mach number is higher than that obtained from the injection index and agrees well with the one derived from the overall spectrum, namely $\mathcal{M} = 3.78^{+0.3}_{-0.2}$. The radio halo shows an average spectral index of $\alpha = -1.16 \pm 0.05$ and a slight gradient from north to south. The southernmost part of the halo is steeper and possibly related to a shock front. Excluding the southernmost part, the halo morphology agrees very well with the X-ray morphology. A power-law correlation is found between the radio and X-ray surface brightness.

Key words: acceleration of particles – galaxies: clusters: individual (1RXS J0603.3+4214) – galaxies: clusters: intracluster medium – large-scale structure of universe – magnetic fields – radiation mechanisms: non-thermal

1. Introduction

Diffuse radio emission, associated with the intracluster medium (ICM), has been observed in a growing number of galaxy clusters, seen as radio relics and radio halos (Feretti & Giovannini 1996; Brüggen et al. 2012; Feretti et al. 2012; Brunetti & Jones 2014). Both of these types of radio sources have a typical size of about 1 Mpc. They show a typical synchrotron spectrum,¹⁰ a clear indication of the existence of cluster-wide magnetic fields and relativistic particles. Both relics and halos are associated with merging clusters (Giacintucci et al. 2008; Cassano et al. 2010; Finoguenov et al. 2010; van Weeren et al. 2011), suggesting that cluster mergers play a major role in their formation.

Radio halos are found at the center of galaxy clusters, have a smooth regular shape morphology, and are usually unpolarized. Most halos are found only in merging systems possessing X-ray substructure (Liang et al. 2000; Cassano et al. 2010; Basu 2012; Cassano et al. 2013). The radio emission from the halo typically follows the X-ray emission from the thermal gas (Govoni et al. 2001b), suggesting a direct connection between the thermal and non-thermal components of the ICM. However, there are also a few systems in which the radio halo emission does not appear to follow the X-ray emission very well—for

example, in the Coma cluster (Brown & Rudnick 2011), Abell 3562 (Giacintucci et al. 2005), and MACSJ0717.5+3745 (Bonafede et al. 2012; van Weeren et al. 2017b).

The cosmic ray electron (CRE) acceleration mechanism responsible for radio halos is still disputed. There are two main models that have been proposed to explain the origin of halos. The primary electron model suggests that relativistic populations of electrons are re-accelerated to higher energies by magneto-hydrodynamical turbulence induced during mergers (Brunetti et al. 2001; Petrosian 2001). The secondary electron model proposes that the CRE are the secondary products of hadronic collisions between thermal ions and relativistic protons present in the ICM (Dennison 1980; Blasi & Colafrancesco 1999; Dolag & Enßlin 2000). The secondary electron model predicts the existence of gamma-rays as one of the products of hadronic collisions. However, the non-detection of gamma-rays in clusters (Jeltema & Profumo 2011; Brunetti et al. 2012; Ackermann et al. 2014, 2016; Brunetti et al. 2017) appears to challenge this model.

Radio relics are large elongated sources located at the periphery of the merging galaxy clusters. Most of them are strongly polarized (Govoni & Feretti 2004; Ferrari et al. 2008), indicating the presence of ordered magnetic fields. They often display irregular morphologies and are believed to be produced by diffusive shock acceleration (DSA) at the merger shocks (e.g., Drury 1983; Enßlin et al. 1998; Roettiger et al. 1999;

¹⁰ $S(\nu) \propto \nu^\alpha$ with spectral index α .

Hoefl & Brüggén 2007; Kang & Ryu 2011). One of the well-studied examples of radio relics is CIZA J2242.8+5301, the “Sausage-relic” (van Weeren et al. 2010; Stroe et al. 2013; Hoang et al. 2017).

There is strong evidence that relics trace shock waves occurring in the ICM during cluster merger events. Cosmological shocks are capable of accelerating electrons (Ryu et al. 2003) to relativistic energies. These electrons, together with magnetic fields of μG -level (Carilli & Taylor 2002, and references therein), emit synchrotron radiation. In the standard scenario for radio relics, particle acceleration (Ensslin et al. 1998) is described by the DSA mechanism. For most of the relics, the observed properties, such as the gradual spectral index steepening toward the cluster center, the high degree of polarization with magnetic field lines parallel to the source extension, and the integrated spectrum with a power-law form, can be well explained by the DSA model.

For several radio relics the jump related to the shock in X-ray surface brightness and temperature has been searched for and identified (Sarazin et al. 2013; Stroe et al. 2013; Shimwell et al. 2015; Eckert et al. 2016; van Weeren et al. 2016). For some relics the derived X-ray Mach numbers are low, posing a severe challenge for the standard scenario for relics (Akamatsu et al. 2012; van Weeren et al. 2016). For weak shocks, namely $\mathcal{M} \lesssim 3$, DSA is inefficient in accelerating particles from the thermal pool to relativistic energies. To solve this low Mach number issue, several alternative models were proposed, such as the shock re-acceleration model (Kang & Ryu 2011; Kang et al. 2012; Pinzke et al. 2013; van Weeren et al. 2017a, 2017b). There are also a few systems where the Mach numbers of the shock waves inferred from X-rays are higher than those inferred from radio observations (Akamatsu et al. 2012; Botteon et al. 2016).

In this work, we present the results of deep L-band VLA observations of the diffuse radio emission associated with the merging galaxy cluster 1RXS J0603.3+4214. We complement our analysis with published LOFAR, GMRT, and *Chandra* observations to study the spectral properties of the radio emission from the cluster and its possible relation to the thermal X-ray emission. We attempt to explain the observed surface brightness profiles by a model using a log-normal magnetic field distribution.

Throughout this paper we assume a ΛCDM cosmology with $H_0 = 71 \text{ km s}^{-1} \text{ Mpc}^{-1}$, $\Omega_m = 0.3$, and $\Omega_\Lambda = 0.7$. At the cluster’s redshift, $1''$ corresponds to a physical scale of 3.64 kpc. All images are in the J2000 coordinate system.

2. 1RXS J0603.3+4214

The galaxy cluster 1RXS J0603.3+4214, located at $z = 0.225$, is known to host three radio relics and a giant elongated radio halo van Weeren et al. (2012a). The most prominent and noticeable radio feature is a large bright relic in the north. It has a peculiar linear morphology, extending to about 1.9 Mpc, with three distinct components resembling the brush (B1) and handle (B2+B3) of a toothbrush. The handle of the Toothbrush is enigmatic because of its large and straight extent and its asymmetric position with respect to the cluster merger axis. Brüggén et al. (2012), using a hydrodynamical N -body simulation, reproduced the elongated linear morphology of the Toothbrush. They showed that a triple merger between two equal mass clusters merging along the north–south axis,

together with a third, less massive, cluster moving in from the southwest, may cause the peculiar shape of the Toothbrush.

For the Toothbrush, van Weeren et al. (2012a) found a relatively flat radio spectral index of $\alpha \approx -0.6$ to -0.7 (between 610 and 325 MHz) at the northern edge. However, recent radio observations indicate a spectral index of $\alpha_{150}^{1500} = -0.80$ (van Weeren et al. 2016). According to standard DSA, this spectral index suggests a Mach number of $\mathcal{M} = 2.8_{-0.3}^{+0.5}$. Stroe et al. (2016) presented the integrated spectrum of the Toothbrush from 150 MHz to 30 GHz and detected a spectral break at frequencies above about 2 GHz. On the other hand, Kierdorf et al. (2016) found that the spectrum can be well-fitted by a single power-law below 8.35 GHz, suggesting that a break in the spectrum does not exist below 8.35 GHz. Basu et al. (2016) studied the impact of the Sunyaev–Zeldovich effect on the observed synchrotron flux and found that the radio spectrum is affected above 10 GHz.

Ogrea et al. (2013) observed the cluster with *XMM-Newton* and found two distinct X-ray peaks and evidence of density and temperature discontinuities, indicating the presence of shocks. The weak-lensing study showed that the cluster is composed of complicated dark matter substructures closely tracing the galaxy distribution (Jee et al. 2016). The cluster mass is dominated by two massive clumps with a 3:1 mass ratio. Recently, *Chandra* observation revealed the presence of a very weak shock of a Mach number of $\mathcal{M} \approx 1.2$ at the other edge of the brush (van Weeren et al. 2016). Clearly, the Mach number of the shock estimated from X-ray observations is lower than that inferred from the observed radio spectral index.

van Weeren et al. (2012a) also found that the cluster hosts a ~ 2 Mpc large giant radio halo. The spectral index map of the halo revealed a remarkably uniform spectral index distribution, namely $\alpha = -1.16$, with an intrinsic scatter of ≤ 0.04 (van Weeren et al. 2016). The halo and the brush region of the Toothbrush seem to be connected by a region with a spectral index of $\alpha = -2.0$, after which the spectrum gradually flattens to $\alpha = -1.0$ and returns to being uniform in the halo. van Weeren et al. (2016) suggested that the flattening of the spectral index is due to the re-acceleration of “aged” electrons downstream of the relic by turbulence, indicating a connection between the northern relic and the halo.

3. Observations and Data Reduction

Observations of the cluster 1RXS J0603.3+4214 were made with the VLA in L-band covering a wide frequency range of 1–2 GHz (project code: SE0737, PI R. J. van Weeren). The L-band observations carried out with A, B, C, and D configurations are summarized in Table 1. The VLA data correspond to a total integration time of around 26 hr on the target. A total bandwidth of 1 GHz was recorded and spread over 16 spectral windows, each divided into 64 channels. All four circular polarization products were recorded. For each configuration, the calibrator 3C147 was observed for around 30 minutes. The second calibrator 3C138 was observed at the end of the target observation for around 15 minutes. In order to cover the largest range of spatial scales and to maximize signal-to-noise, we combine all four VLA configurations data sets for imaging.

The data were calibrated and reduced with the CASA¹¹ package (McMullin et al. 2007), version 4.6.0. Initially, the

¹¹ <http://casa.nrao.edu/>

Table 1
VLA L-band Observations Overview

	A-configuration	B-configuration	C-configuration	D-configuration
Observation Dates	2012 Dec 8	2013 Nov 30	2013 Jun 17	2013 Jan 28
Frequency Range	1–2 GHz	1–2 GHz	1–2 GHz	1–2 GHz
Integration Time	1 s	3 s	5 s	5 s
On Source Time	4 + 4 hr	8 hr	6 hr	4 hr

Note. For all configurations, the number of spectral widows is 16, the number of channels per spectral window is 64, and the channel width is 1 MHz. Full Stokes polarization information was recorded.

data obtained from the four different configurations were separately calibrated. The first step of data reduction consisted of the Hanning smoothing of data. After this, we determined and applied elevation dependent gain tables and antenna offset positions. The data were then inspected for Radio Frequency Interference (RFI) removal. The `CASA tfcrop` mode was used for automatic flagging of strong narrow-band RFI. We then corrected for the bandpass using the calibrator 3C147. This prevents flagging of good data due to the bandpass roll-off at the edges of the spectral windows. The low amplitude RFI was searched for and flagged using `AOFlagger` (Offringa et al. 2010). The amount of data affected by RFI was typically only a few percent in A and B configurations, but significant interference was encountered in C and D configurations.

As a next step in the calibration, we used the L-band 3C147 model provided by the `CASA` software package and set the flux density scale according to Perley & Butler (2013). An initial phase calibration was performed using both the calibrators for a few neighboring channels per spectral window, where the phase variations per channel were small. We corrected for the antenna delay and determined the bandpass response using the calibrator 3C147. After applying the bandpass and delay solutions, we proceeded to the gain calibration for both the calibrators. In the end, all relevant calibration solutions were applied to the target data. The resulting calibrated data were averaged by a factor of 4 in frequency per spectral windows and in time intervals of 10 s, 10 s, 6 s, and 4 s for D, C, B, and A configurations, respectively.

After initial imaging of the target field, for each configuration, we carried out a self-calibration first with a few rounds of phase-only calibration followed by a final round of amplitude-phase calibration. For A and B configurations, we performed an additional bandpass calibration on the target, using the target field model derived from the self-calibration, which reduced the dynamic range. We visually inspected the self-calibration solutions and manually flagged some additional data. For wide-field imaging, we employed W-projection algorithm (Cornwell et al. 2008) to correct for non-coplanarity. We imaged each configuration using `nterms` = 3 (Rau & Cornwell 2011) to take into account the spectral behavior of the bright sources. The deconvolution was always performed with `CLEAN` masks generated in the `PyBDSF` (Mohan & Rafferty 2015). We used the Briggs weighting scheme with a `robust` parameter of 0.

After deconvolving each configuration independently, we subtracted from the uv-data three bright sources (labeled as A, V, and U in Figure 1). Next, for each configuration, we made a single deep Stokes I continuum image using the full bandwidth with `nterms` = 2 that reduced the noise level by about 30%–40%. To speed up imaging, we subtracted in the uv-plane all sources outside a cluster region.

Finally, the A, B, C, and D configurations data were combined together to make a single deep full bandwidth Stokes I image, using multi-scale clean (Rau & Cornwell 2011) and `nterms` = 2. An overview of the image properties is given in Table 2. The output images were corrected for primary beam attenuation.

We assume an absolute flux calibration uncertainty of 4% for the VLA L-band (Perley & Butler 2013). For any flux density measurement, we estimate the uncertainty via

$$\Delta S = \sqrt{(0.04S)^2 + N_{\text{beams}} (\sigma_{\text{rms}})^2}, \quad (1)$$

where S is the flux density, σ_{rms} is the rms noise, and N_{beams} is the number of beams. We list configuration, resolution, imaging parameters, and achieved noise level in Table 2. All the VLA images, unless otherwise noted, were made using data from all four configurations.

4. Results: VLA Radio Continuum Images

We show in Figure 1 the resulting 1–2 GHz VLA radio continuum images of 1RXS J0603.3+4214 created with different uv-tapers. The known diffuse emission features, namely the bright Toothbrush, the two radio relics to the west, and the large elongated halo, are evidently recovered in our observation. The sources are labeled following van Weeren et al. (2012a) and extending the list. The properties of compact and diffuse sources in the cluster are summarized in Tables 3 and 4.

4.1. Radio Relics

A high resolution VLA image of the Toothbrush with a restoring beam of $1''.96 \times 1''.52$ is shown in Figure 2. The complex, often filamentary structures in the Toothbrush at this resolution are one of the relic’s most striking features. We briefly describe prominent features seen in Figure 2. The brush shows a distinct, more or less narrow ridge to the north with a quite sharp outer edge. At the narrowest location, the ridge has a width of about 25 kpc.

To even better identify structures across the ridge, we further increased the resolution using only A and B configurations and achieving a restoring beam of $1''.07 \times 0''.97$ (see Figure 3). Interestingly, the ridge seems to consist of two parts that branch to the west, labeled as ridge branches in Figure 3 panel (a). The surface brightness downstream of the ridge drops very quickly in our image, while at low frequencies (150 and 610 MHz), the surface brightness decreases more gradually (van Weeren et al. 2012a, 2016).

The brush shows small filaments, “bristles,” which are arc-shaped and more or less perpendicular to the ridge. The width of the bristles is about 3–5 kpc. At 610 and 150 MHz, van Weeren et al. (2012a, 2016) found several

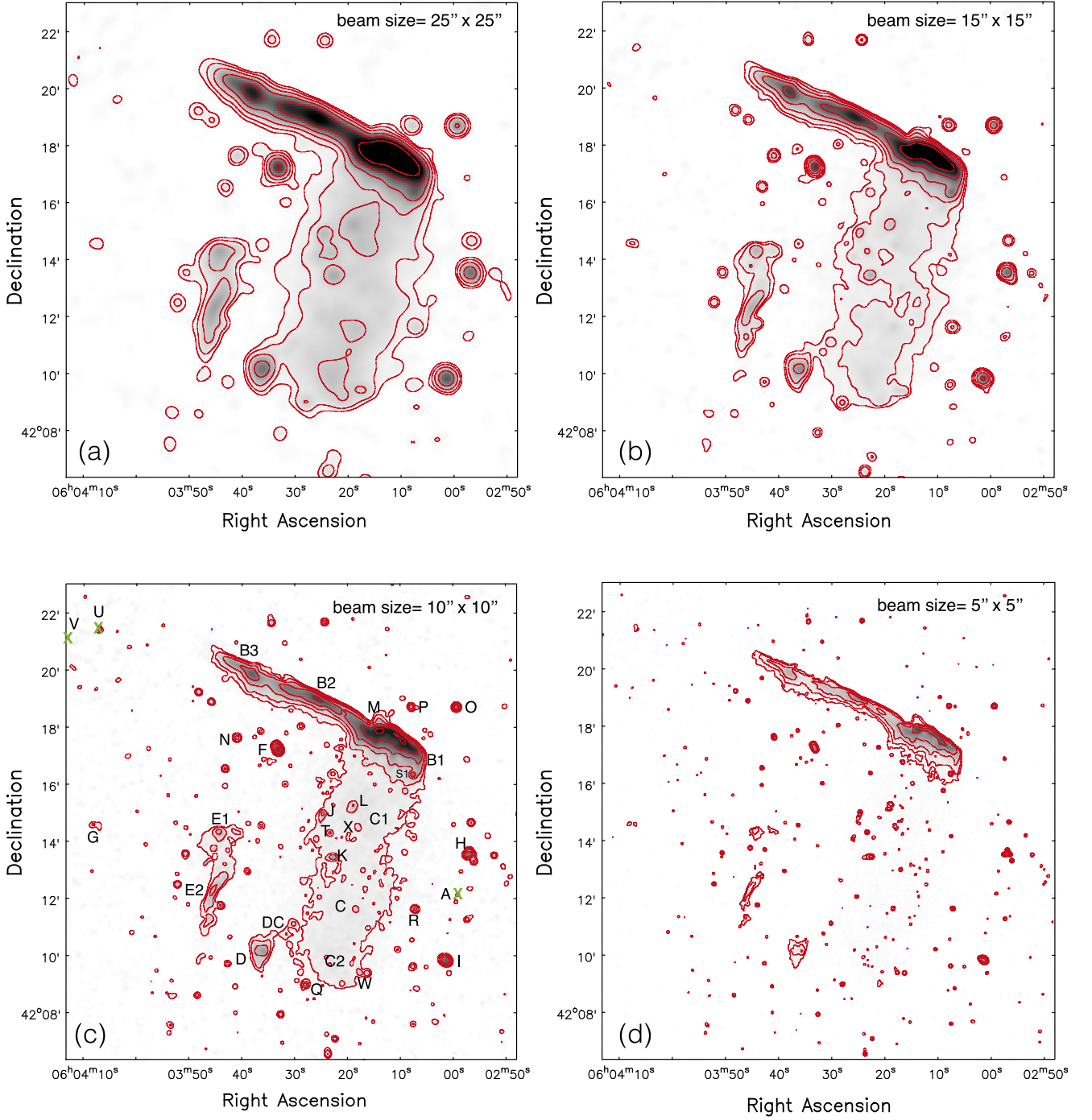


Figure 1. VLA 1–2 GHz images of 1RXS J0603.3+4214 at different resolutions. In all four images, the known relics (B, D, and E) are evidently recovered. The image properties are given in Table 2. Here, panel (a), (b), (c), and (d) correspond to IM15, IM13, IM10, and IM4, respectively. Contour levels are drawn at $[1, 2, 4, 8, \dots] \times 4.5 \sigma_{\text{rms}}$. In these images there is no region below $-4.5 \sigma_{\text{rms}}$, except a small area close to the subtracted source A. The green cross marks the exact location of the sources which have been subtracted, namely A, U, and V.

“streams” of emission, wider than the bristles, extending from the northern part of B1 to the south. These streams are also visible in the VLA 1–2 GHz image (see Figure 2). To the northeast of B1, we confirm the low surface brightness emission, source M, reported by van Weeren et al. (2012a).

The origins of the filamentary structures, the ridge and the bristles, are not known. For Abell 2256, Owen et al. (2014) reported many long pronounced filaments stretching across the entire relic, which are presumably seen face-on. The ridge and

the bristles are possibly caused by similar filaments. In contrast to the relic in Abell 2256, the Toothbrush is seen edge-on; hence the bristles could be the ends of filaments stretched across the entire relic.

Another distinctive morphological feature is the double strand, emerging from B1, see Figure 2. The intrinsic width of these strands varies from 30 to 17 kpc when moving from west to east. The two strands merge at $06^{\text{h}}03^{\text{m}}25^{\text{s}} + 42^{\circ}18'59''$, and further to the east there seem to be several strands again. It appears as if the strands were twisted (Figure 2).

Table 2
Image Properties

Name ^a	Configurations ^b (VLA)	Restoring Bbeam	Weighting	uv Cut	uv-taper	Rms Noise (VLA)	Rms Noise (GMRT)	Rms Noise (LOFAR)
IM1	AB	1''07 × 0''97	Briggs	none	none	2 μJy
IM2	ABCD	1''96 × 1''52	Briggs	none	none	6 μJy
IM3	ABCD	3''5 × 3''5	Briggs	none	4''	7 μJy
IM4	ABCD	5''0 × 5''0	Briggs	none	6''	6 μJy
IM5	ABCD	5''5 × 5''5	uniform	none	6''	7 μJy
IM6	ABCD	5''5 × 5''5	uniform	≥0.2 kλ	6''	7 μJy	...	144 μJy
IM7	ABCD	5''5 × 5''5	uniform	≥0.9 kλ	6''	8 μJy	60 μJy	170 μJy
IM8	ABCD	6''5 × 6''5	uniform	≥0.2 kλ	8''	8 μJy	...	155 μJy
IM9	ABCD	7''0 × 7''0	Briggs	none	8''	8 μJy
IM10	ABCD	10'' × 10''	Briggs	none	10''	11 μJy
IM11	ABCD	11'' × 11''	uniform	none	10''	11 μJy
IM12	ABCD	11'' × 11''	uniform	≥0.2 kλ	10''	12 μJy	...	176 μJy
IM13	ABCD	15'' × 15''	Briggs	none	16''	16 μJy
IM14	ABCD	16'' × 16''	uniform	≥0.2 kλ	16''	18 μJy	...	208 μJy
IM15	ABCD	25'' × 25''	Briggs	none	25''	24 μJy	...	190 μJy
IM16	ABCD	25'' × 25''	uniform	none	25''	26 μJy	...	193 μJy

Notes. Imaging was always performed using multi-scale clean, $n_{\text{terms}} = 2$, and $w_{\text{projplanes}} = 500$. For all images made with Briggs weighting, we used $\text{robust} = 0$.

^a Image name.

^b uv-data of configuration combined for imaging.

Table 3
Flux Density of Compact Sources in the Cluster Region

Source	$S_{1.5 \text{ GHz}}$ mJy	Type
A	286.0 ± 28.0	quasar
F	5.78 ± 0.27	double-lobed
G	4.44 ± 0.32	double-lobed
H	2.52 ± 0.23	double-lobed
I	4.27 ± 0.53	spiral-galaxy
J	0.58 ± 0.17	head–tail
K	0.95 ± 0.21	head–tail
L	0.62 ± 0.22	...
N	0.65 ± 0.12	spiral-galaxy
O	1.72 ± 0.20	spiral-galaxy
P	0.58 ± 0.13	...
Q	0.43 ± 0.09	...
R	0.38 ± 0.08	...
S1	1.46 ± 0.09	...
T	0.33 ± 0.07	...
U	24.80 ± 2.10	double-lobed
V	65.60 ± 6.01	double-lobed
W	0.30 ± 0.07	head–tail
X	0.25 ± 0.06	...

Note. Flux densities are measured in the image IM4, see Table 2. The type is determined from the radio morphology and the presence of an optical counterpart.

Interestingly, the highest resolution image reveals that in the twist region one of the strands actually consists of two thin parallel threads with a separation of about 1''3 corresponding to 5 kpc, shown in Figure 3 panel (b).

The B3 part of the handle seems to consist of one filament running from east to west and one that runs arc-shaped from north to south. The highest surface brightness is found where the filaments cross. We denote this region as the “junction” (Figure 2). With a surface brightness close to the noise, a structure is tentatively visible that connects the northern tip of

the junction and one end of the strands, therefore denoted as “bridge”; see Figure 3 panel (c).

The radio relic E, located on the eastern side of the cluster center, is shown in Figure 1. It consists of two parts, E1 and E2. The total extent of E, from north to south, is about 5'2, corresponding to a physical size of 1.1 Mpc.

The high resolution image of relic E is shown in Figure 4. The three bright regions of relic E, labeled as EA, EB, and EC, are surrounded by low surface brightness emission. For none of the three regions can we identify a related radio galaxy. However, there are several radio galaxies embedded within relic E, marked with the green circles in Figure 4, but they do not appear to be connected with these three bright regions. This underlines that all three regions are diffuse emission.

Another diffuse emission region has been classified as a relic, namely source D, located southwest of relic E. We recover a similar morphology as found by van Weeren et al. (2012a) using GMRT 610 MHz data. Part of the emission resembles a bullet with a Mach cone; see Figure 4. Moreover, relic D is apparently connected to the halo via patchy emission DC; see Figure 1.

Recently, evidence has been found that radio relics may originate from a combination of outflows of radio galaxies and the impact of a merger shock (van Weeren et al. 2017a). Relics E and D show a quite unusual morphology; however, we do not find any connection to a nearby radio galaxy.

4.2. Radio Halo

The VLA images also recover the extended radio halo emission, as shown in Figure 1. The halo emission is not detected at very high resolution (e.g., Figure 1 panel (d)), due to its low surface brightness. However, we can use the sensitive high resolution image to identify faint compact sources in the halo region, which may contribute to the total flux density measured at the lower resolution.

The shape of the halo in the VLA images is similar to the low frequency images (van Weeren et al. 2012a, 2016),

Table 4
Flux Densities and Integrated Spectra of the Diffuse Radio Sources in the Cluster 1RXS J0603.3+4214

Source	VLA			GMRT	LOFAR		LLS	α_{150}^{1500}	\mathcal{M}
	25"	5"5 and 11"	5"5 and 11"	5"5	25"	5"5 and 11"	Mpc		
	$S_{1.5 \text{ GHz}}$ mJy	$S_{1.5 \text{ GHz}}$ mJy	$S_{1.5 \text{ GHz}}$ mJy With uv Cut	$S_{610 \text{ MHz}}$ mJy With uv Cut	$S_{150 \text{ MHz}}$ mJy	$S_{150 \text{ MHz}}$ mJy With uv Cut			
(1)	(2)	(3)	(4)	(5)	(6)	(7)	(8)	(9)	(10)
relic B	310.0 ± 21	296.0 ± 17.0	258.0 ± 14.0	751.0 ± 78.0	4428.0 ± 410.0	3669.0 ± 378.0	1.9	-1.15 ± 0.02	$3.78^{+0.3}_{-0.2}$
halo C	33.4 ± 2.7	31.6 ± 2.6	30.0 ± 1.2	...	490.0 ± 56.0	441.0 ± 44.0	1.7 ^a	-1.17 ± 0.04	...
relic D	5.2 ± 0.8	4.9 ± 0.7	4.6 ± 0.2	13.0 ± 1.7	98.1 ± 11.8	87.1 ± 9.1	0.3	-1.28 ± 0.05	...
relic E	11.6 ± 1.3	10.1 ± 1.2	9.0 ± 0.3	18.7 ± 2.2	153.1 ± 13.0	115.2 ± 11.8	1.1	-1.11 ± 0.05	$4.3^{+1.4}_{-0.7}$
region S	9.1 ± 1.1	8.4 ± 1.0	7.7 ± 0.3	...	172.0 ± 18.8	148.0 ± 15.0	0.7	-1.28 ± 0.05	...

Note. The regions where the fluxes were extracted are indicated in Figure 7, right panel. Column (1) gives the source name; Column (2) gives flux densities measured from the IM16 (see Table 2 for image properties); Column (3) gives flux densities measured in IM5 and IM11 for relics and halo/region S, respectively; Column (4) gives flux densities measured in IM7 and IM12 for relics and halo/region S; Column (5) gives flux densities measured from the GMRT image with properties given in Column (4); Column (6) gives flux densities measured from the LOFAR image with properties given in Column (2); Column (7) gives flux densities measured from the LOFAR image with properties given in Column (4); Column (8) gives the largest linear size at 1.5 GHz; Column (9) gives the integrated spectral indices between 150 MHz and 1.5 GHz obtained by fit to Column (4), Column (5), and Column (7). We assume an absolute flux-scale uncertainty of 10% for the GMRT and LOFAR data, and 4% for the VLA data. Column (10) gives the Mach numbers derived from the integrated spectrum given in Column (9).

^a Size of the entire halo C.

elongated along the merger direction. At 1–2 GHz, the radio halo has a largest angular size of about $8'.7$, corresponding to a physical extent of 1.7 Mpc.

In the VLA image there is a slight decrease in the surface brightness, apparently separating the relic and the halo. It is also worth noting that the transition from halo to relic (i.e., which type of diffuse emission dominates the surface brightness) appears in the VLA image at a different location than in the LOFAR image; see Figure 5.

In our sensitive high resolution radio maps, we detected 32 discrete sources ($>5\sigma_{\text{rms}}$) within the halo region, including several head–tail radio galaxies. These sources were not detected in previously published observations. Without subtracting the 32 sources, the measured flux density of the halo region at $10''$ resolution (IM10) is 53.0 ± 4.0 mJy. We measure the flux density for the entire halo C. The combined total flux density of the 32 discrete sources is ~ 13 mJy, which means $\sim 25\%$ of total flux resides in these sources. The flux density of the halo hence amounts to $S_{1.5 \text{ GHz}}^{\text{halo}} \sim 40.0$ mJy. We also confirm that the southern part of the radio halo shows a sharp outer edge, as reported by van Weeren et al. (2016).

4.3. Optical, X-Ray, and Radio Continuum Overlay

The cluster 1RXS J0603.3+4214 was observed with the 8.2m Subaru telescope on 2013 February 25 in r, g, and i colors for 2880 s, 720 s, and 720 s, respectively (Jee et al. 2016). The X-ray emission of the cluster was observed with ACIS-I *Chandra* telescope (210 ks) in 2013 in the 0.5–2.0 keV band (van Weeren et al. 2016). The spectroscopic redshifts of the sources in the field were taken from Subaru observations (W. A. Dawson et al. 2017, in preparation).

We create an overlay of the optical, X-ray, and radio emission in the cluster region using a Subaru composite image, the *Chandra* X-ray image, and our VLA 1–2 GHz radio continuum image; see Figure 6. To see the radio emission nicely, in particular the filamentary structures associated with the Toothbrush, we convolve the VLA image $1''.96 \times 1''.52$ image to $3''.5 \times 3''.5$.

For relic E, point sources for which we found an optical counterpart are denoted with green circles in Figure 4. We do not find an optical counterpart for the brightest regions of relic E (i.e., for EA, EB, and EC), which could be assumed to be the source of the radio emission in these regions.

5. Analysis and Discussion

To study the spectral characteristics of the cluster radio emission, we use the VLA 1–2 GHz, the GMRT 610 MHz and the LOFAR 120–181 MHz observations. The GMRT and LOFAR data sets were originally published by van Weeren et al. (2012a, 2016). We also use *Chandra* observations to study the X-ray emission from 1RXS J0603.3+4214. For data reduction steps, we refer to van Weeren et al. (2012a, 2016).

The radio observations reported here were performed using three different interferometers, each of which has different uv-coverages. This results in a bias in the total flux density measurements, the integrated spectra, and the spectra index maps. To overcome these biases, we create images at 150 MHz, 610 MHz, and 1.5 GHz, with a common minimum uv cut and uniform weighting. Imaging is always performed with multi-scale clean and $n_{\text{terms}} = 2$. To reveal spectral properties of different spatial scales, we tapered images accordingly. The imaging parameters and the image properties are summarized in Table 2.

5.1. Flux Measurements and Integrated Radio Spectra

It is difficult to accurately measure the flux density of extended low surface brightness sources in interferometric data. There are several reasons: first of all, if short baselines are missing or cut in the uv-data, the flux of extended structures gets “resolved out.” Also, the distribution of antenna and the resulting uv-coverage may affect the flux measurement. Finally, structures with a surface brightness close to the noise level are notoriously difficult to deconvolve; the resulting flux measurements are very uncertain. Therefore, the deconvolution becomes particularly challenging for high resolution images.

We investigate here how the measured flux densities change when using different imaging parameters—for example, uv cut

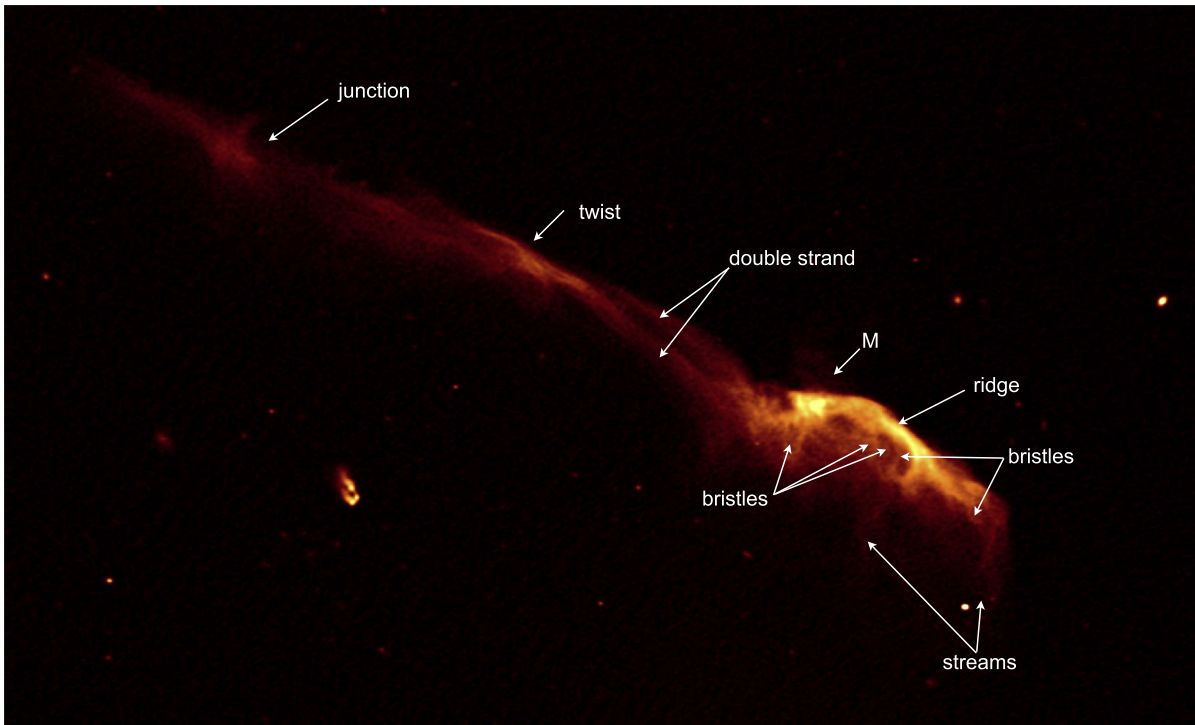


Figure 2. High resolution VLA 1–2 GHz image of the Toothbrush showing the complex, often filamentary structures. The image properties are given in Table 2, IM2.

and resolution. In Table 4, we report the flux measurement of several regions. The flux densities reported in this section, unless stated otherwise, are measured from radio maps imaged with uniform weighting (Stroe et al. 2016). The VLA low resolution image made with all configurations and without any uv cut gives the maximum flux values. For instance, for relic B the flux density measured from the $25''$ resolution map is 310 ± 21 mJy. The flux density of the same region when measured from the $5''5$ resolution image is 296 ± 17 mJy. This means that the increase in the image resolution results in a 5% flux loss. However, the image made using the same resolution but with a common inner uv cut of $0.9 \text{ k}\lambda$ gives a flux density of 258 ± 14 mJy. Hence, the uv cut causes an additional flux loss of about 15%. In total, 20% of the flux density reduction is caused by the resolution and the uv cut. For the LOFAR and GMRT data, we notice the same flux density reductions (e.g., without any uv cut, the flux density of relic B at 150 MHz is 4428 ± 410 mJy, and with a uv cut it is 3669 ± 378 mJy). Therefore, to ensure that we recover flux on the same spatial scales, we produce images with a common lower uv cut of $0.9 \text{ k}\lambda$. Here, $0.9 \text{ k}\lambda$ is the minimum uv-distance of the GMRT data. We also measure the flux densities from the $40''$ maps. The obtained flux densities are only marginally higher than the values reported in Table 4 at $25''$ resolution. To obtain the integrated spectrum of sources, we prefer high resolution imaging where it is easier to separate the source emission from other complex sources. The low resolution is not preferred, because it is hard to decide the regions where to measure the flux density. We note that for all images, multi-scale clean has been used. Although we lose some flux, less than 5% as mentioned previously, when measuring the flux density from higher resolution images, this effect remains the same for all data sets and will not affect the integrated spectral index calculations.

According to the DSA theory, the particle acceleration at the shock front is determined by the Mach number of the shock (Blandford & Eichler 1987). More precisely, DSA in the test-particle regime generates a population of relativistic electrons with a power-law energy distribution $\partial N / \partial E \propto E^{-\delta_{\text{inj}}}$. The resulting radio spectrum is a power-law with index $\alpha_{\text{inj}} = -(\delta_{\text{inj}} - 1)/2$ and reflects the Mach number of the shock front,

$$\mathcal{M} = \sqrt{\frac{2\alpha_{\text{inj}} - 3}{2\alpha_{\text{inj}} + 1}}, \quad (2)$$

where α_{inj} is the injection spectral index. For a stationary shock in the ICM (i.e., the electron cooling time is much shorter than the timescale on which the shock strengths or geometry changes), the integrated spectrum, α_{int} , is by 0.5 steeper than the injection spectrum,

$$\alpha_{\text{int}} = \alpha_{\text{inj}} + 0.5. \quad (3)$$

Recent simulations by Kang (2015) suggest that merger shocks might not be considered as stationary. The resulting spectra would be curved. We investigate here the integrated spectra of the relics and the halo.

The radio spectrum of the Toothbrush has been studied extensively. van Weeren et al. (2012a) reported that the integrated spectrum from 74 MHz to 4.9 GHz has a power-law shape with $\alpha_{\text{int}} = -1.10 \pm 0.02$. Stroe et al. (2016) studied the integrated spectrum from 150 MHz to 30 GHz, using a uv cut of $0.8 \text{ k}\lambda$, and detected a spectral steepening above about 2 GHz. They reported that the spectral index steepens from $\alpha = -1.00$ to $\alpha = -1.45$. Recently, Kierdorf et al. (2016) studied the Toothbrush at 4.85 and 8.35 GHz with the 100 m Effelsberg telescope and found a power-law spectrum with index $\alpha = -1.0 \pm 0.04$ up to 8.35 GHz. Hence it remains

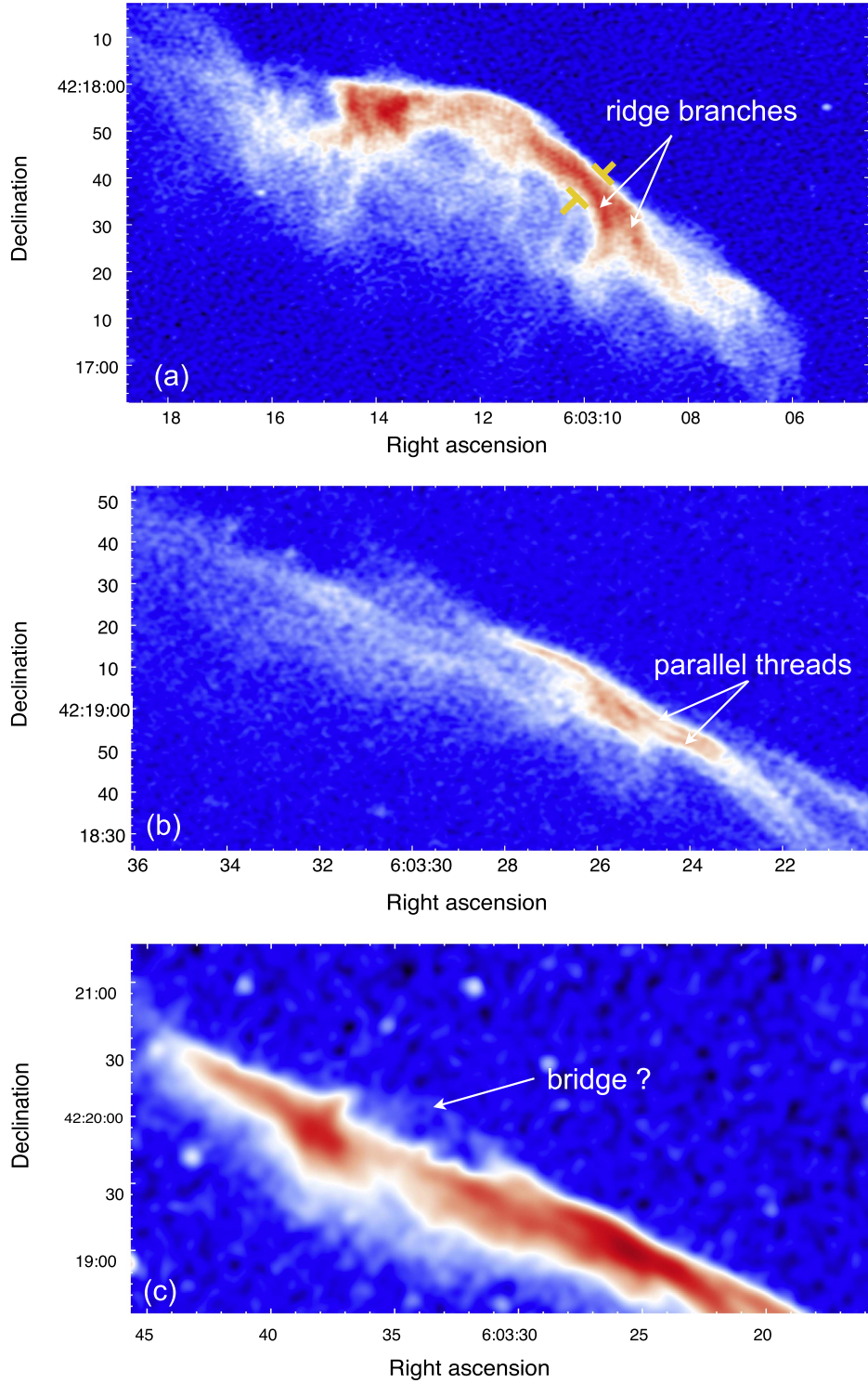


Figure 3. VLA 1–2 GHz images of different regions of the Toothbrush. Top: cut out around the B1 region, showing that the ridge consists of two parts that branch to the west. The ridge has a width of about 25 kpc, measured across the region marked with yellow. The image properties are given in Table 2, IM1. Middle: cut out around the center of B2 region (twist), revealing two very thin parallel filaments that are separated by 5 kpc. The image properties are given in Table 2, IM2. Bottom: bridge connecting the B3 region of relic to B2. The image properties are given in Table 2, IM4.

unclear if the integrated spectrum of the Toothbrush is curved at high frequencies.

To obtain the integrated spectra of relics, we convolved the LOFAR, GMRT, and VLA images to the same beam size of $5''.5 \times 5''.5$. The regions where the fluxes were extracted are indicated in Figure 7 right panel. We note that there is a region which belongs to the relic according to the surface brightness at

150 MHz but at 1.5 GHz to the halo. This region is denoted as “relic+halo” in Figure 5. When determining the integrated spectrum, this region is considered as the part of relic B because in the VLA high resolution images (e.g., in Figure 1 panel (d)), this region does not contribute much to the total flux and will not significantly affect our measurements. We will argue in Section 5.5 that the southern part of the halo, denoted

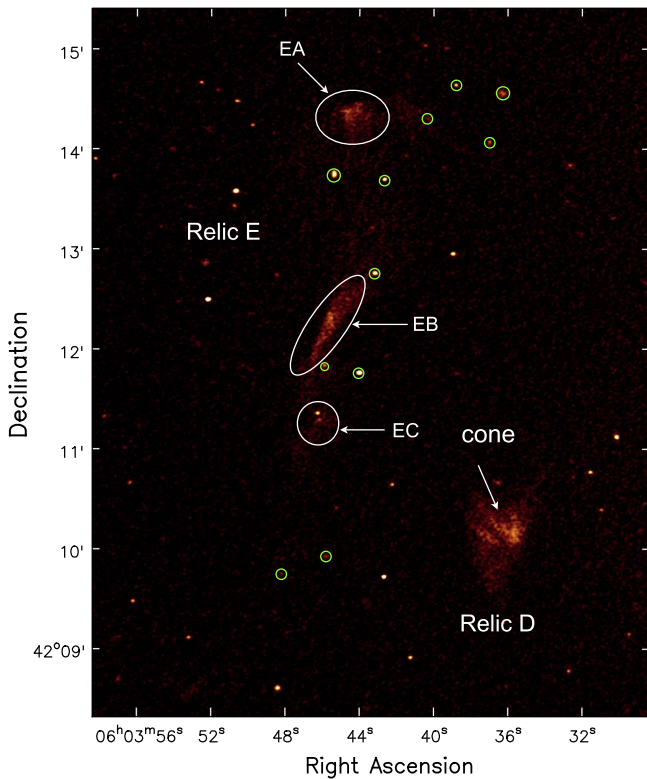


Figure 4. High resolution VLA 1–2 GHz image of relics E and D. The image properties are given in Table 2, IM2. The three bright compact regions EA, EB, and EC are surrounded by diffuse low surface brightness emission. The point sources embedded within relic E, which are clearly detected at 1.5 GHz with optical counterparts visible in the Subaru image, are marked with green circles.

as “region S” in Figure 5, may have a different origin. Hence, we exclude this as well as the “relic+halo” region when computing the halo spectrum.

The radio halo and region S are not detected in the high resolution GMRT 610 MHz image. Therefore, to obtain the integrated spectra of the radio halo and region S, we create new radio maps at 150 MHz and 1.5 GHz using a common lower uv cut of $0.2 \text{ k}\lambda$ to match the scale of the VLA with LOFAR. We then convolve the LOFAR and VLA images to the same beam size of $11'' \times 11''$.

The integrated synchrotron spectra for relics B, D, and E obtained by combining our measured flux densities at frequencies 150 MHz, 610 MHz, and 1.5 GHz are shown in Figure 7, left panel. For the Toothbrush, we find a spectral index of -1.15 ± 0.02 , which is consistent with the previous values of -1.10 ± 0.02 (van Weeren et al. 2012a) and -1.09 ± 0.05 (van Weeren et al. 2016). The spectrum is fitted well by a single power-law, and we do not find any evidence for a spectral steepening in this frequency range. Using Equations (2) and (3), we derive a Mach number of $\mathcal{M} = 3.78^{+0.3}_{-0.2}$.

For relic E, we measure an integrated spectral index of -1.11 ± 0.05 , yielding a Mach number of $4.3^{+1.4}_{-0.7}$. The integrated spectral index of relic D is -1.28 ± 0.05 .

For a few relics, the injection spectral indices derived from the integrated spectral indices are even flatter than allowed by DSA test-particle theory—that is, spectra have been found flatter than -0.5 , for example, in A2256 (van Weeren et al. 2012b; Trasatti et al. 2015) and CIZA J2242.8+5301

(Kierdorf et al. 2016; Hoang et al. 2017). The derived integrated spectral index of relics B, D, and E is consistent with the DSA approximation.

A steepening of the halo spectrum with frequency is noticed in Abell 3562 and Abell 2256 (Giacintucci et al. 2005; van Weeren et al. 2012b). The turbulent acceleration model with particles emitting in a region with relatively uniform magnetic field intensity was invoked to explain the high frequency steepening in Abell 3562, while the low frequency steepening in Abell 2256 was explained with inhomogeneous turbulence. For the radio halo in 1RXSJ0603.3+4214, we find an integrated spectral index of -1.17 ± 0.04 .

The integrated spectral index of the southernmost part of the halo, labeled as “region S” in Figure 5, is -1.28 ± 0.05 , indicating that this region is steeper than the rest of the halo.

It is worth to emphasizing that the radio spectrum of relics B, D, and E are well described by a single power-law spectrum, and the flux densities presented here have been measured from high resolution images that were created using the same uv cut and weighting scheme at all frequencies.

5.2. Analysis of the Relics

The Toothbrush is known to show a clear spectral index gradient (van Weeren et al. 2012a). This is believed to reflect the aging of the relativistic electron population while the shock front propagates outwards (van Weeren et al. 2010). However, it is worth noting, Skillman et al. (2013) found in simulations that relics can show a similar spectral index gradient, despite no inclusion of spatially resolved spectral aging in the model. In these simulations, the spectral index gradient is caused by a variation of the Mach number across the shock surface.

In van Weeren et al. (2016), a high resolution spectral index map of the Toothbrush was derived using the LOFAR 150 MHz and GMRT 610 MHz data. The latter restricted the spectral index map resolution to $6''/5$. Our VLA data allow us to reconstruct the surface brightness distribution at 1.5 GHz with a higher resolution; hence we aim for high frequency spectral index maps, using LOFAR and VLA data, with the best resolution possible.

We briefly describe how we created the spectral index maps. We apply an inner uv cut of $0.2 \text{ k}\lambda$ to the LOFAR data. This ensures that “resolving out” a possible large-scale flux distribution has a similar effect on both data sets. Here, $0.2 \text{ k}\lambda$ is the minimum uv-distance in the VLA data set. For imaging, we use uniform weighting and allow for spectral slopes ($n_{\text{terms}} = 2$). Due to different uv-coverages of the LOFAR and VLA data, the resulting images have slightly different resolution. Therefore, we convolve the VLA image to LOFAR resolution (i.e., $5''/5$). To have the same pixel position in both the images, we use the CASA task `imregrid`. Pixels with a flux density below $5 \sigma_{\text{rms}}$ in either image were blanked. Finally, we computed pixel-wise the spectral index maps.

To derive the spectral index uncertainty map, we take into account the image noise and the absolute flux calibration uncertainty. The flux-scale uncertainty f_{err} of VLA L-band is about 4% (Perley & Butler 2013), and for LOFAR we assume it to be 10%. We estimate the spectral index error via

$$\Delta\alpha = \frac{1}{\ln\left(\frac{\nu_1}{\nu_2}\right)} \sqrt{\left(\frac{\Delta S_1}{S_1}\right)^2 + \left(\frac{\Delta S_2}{S_2}\right)^2}, \quad (4)$$

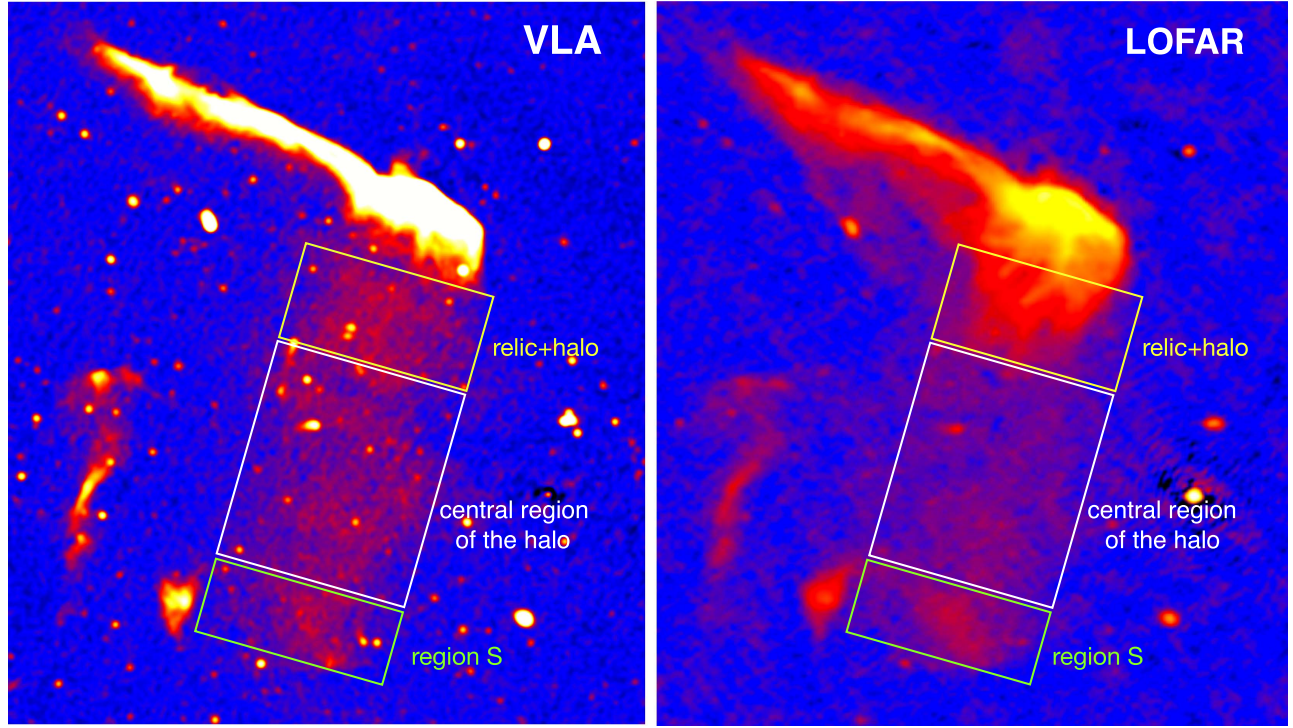


Figure 5. Comparison of the halo between the VLA 1–2 GHz and the LOFAR 120–181 MHz image (van Weeren et al. 2016). Both the images have similar resolution; the VLA image properties are given in Table 2, IM9. To compare radio morphologies at these two frequencies, the colors in both images were scaled manually. In both images, the yellow rectangular box indicates the “relic+halo” region (here, relic+halo indicates that in the VLA and LOFAR image the halo and relic surface brightness dominates, respectively). The southernmost part of the halo is denoted as region S. We define that region of the halo which excludes the relic+halo region and region S as the “central region.”

where S_1 and S_2 are the flux density values at each pixel in the VLA and LOFAR maps at the frequencies $\nu_1 = 1500$ MHz and $\nu_2 = 150$ MHz. ΔS_1 and ΔS_2 were calculated as

$$\Delta S_j = \sqrt{(f_{\text{err}} \times S_j)^2 + (\sigma_{\text{rms}}^j)^2}, \quad (5)$$

where $j \in 1, 2$ and σ_{rms}^j is the corresponding rms noise in the image.

The $5''.5$ resolution spectral index map of the Toothbrush between 150 MHz and 1.5 GHz is shown in Figure 8. The map evidently confirms the remarkably uniform spectral steepening perpendicular to the relic extension, varying roughly from -0.68 to -2.0 . These values are in agreement with van Weeren et al. (2016). The B2 region, where the double strand appears twisted, shows the flattest spectral index, namely $\alpha = -0.68 \pm 0.06$. The B3 region also shows few patches of flat spectral index.

From our high resolution spectral index map, interesting details become visible: at the ridge the spectral index is apparently flatter than reported earlier (van Weeren et al. 2016), namely $-0.70 \leq \alpha \leq -0.80$. Interestingly, the spectrum already steepens across the ridge from $\alpha = -0.70$ to -0.96 . In the double strand, it becomes evident that at the northern strand the spectral index is flatter, and downstream of it, the spectrum is steeper. Surprisingly, at the southern strand the spectrum again gets flatter. The change in the spectral index across the double strand might be due to a new injection. Another possible explanation for the change of the spectral index across the double strand is an increase in strength of the local magnetic field, which brightens up the emission and flattens the spectrum. We confirm the spectral index steepening along the “streams” of emission that emerges from the brush,

reported by van Weeren et al. (2016). A clear north–south gradient is also seen across the streams, with steepening up to -2.0 ± 0.10 at the southern ends. However, there is no evidence of the spectral index flattening at the southern end of the streams, as found by van Weeren et al. (2016).

We investigate the spectral index distribution along the northern edge of the Toothbrush, with distance increasing from east to west. We determine the spectral indices in small square regions (see Figure 9 right panel), with sizes approximately equal to the restoring beam size of the map (i.e., $5''.5$). The extracted spectral indices are shown in the Figure 9 left panel with black dots. The spectral index varies mainly between -0.70 and -0.90 , with brighter parts corresponding to flatter spectra. At the shock front, we find that the spectral index is roughly about -0.75 , which is consistent with what we estimated from the spectral index maps. However, as mentioned previously, these values are slightly flatter than reported by van Weeren et al. (2016). To compare our spectral index map with that of van Weeren et al. (2016), we also create a spectral index map at a $6''.5$ resolution. Such a comparison will also show the impact of the resolution on the spectral indices.

The magenta dots in Figure 9 left panel show the variation of the spectral index extracted from the $6''.5$ resolution map. It is evident that the spectral index at the location of shock front, in this case, is about -0.80 and is consistent with van Weeren et al. (2016). Evidently, there is a shift in the spectral indices across the entire radio relic caused by lowering the resolution. This raises the question of how we can identify the actual injection spectrum at the shock front. The resolution study presented here indicates that the spectral index flattens with increasing resolution; hence with an even better resolution, we

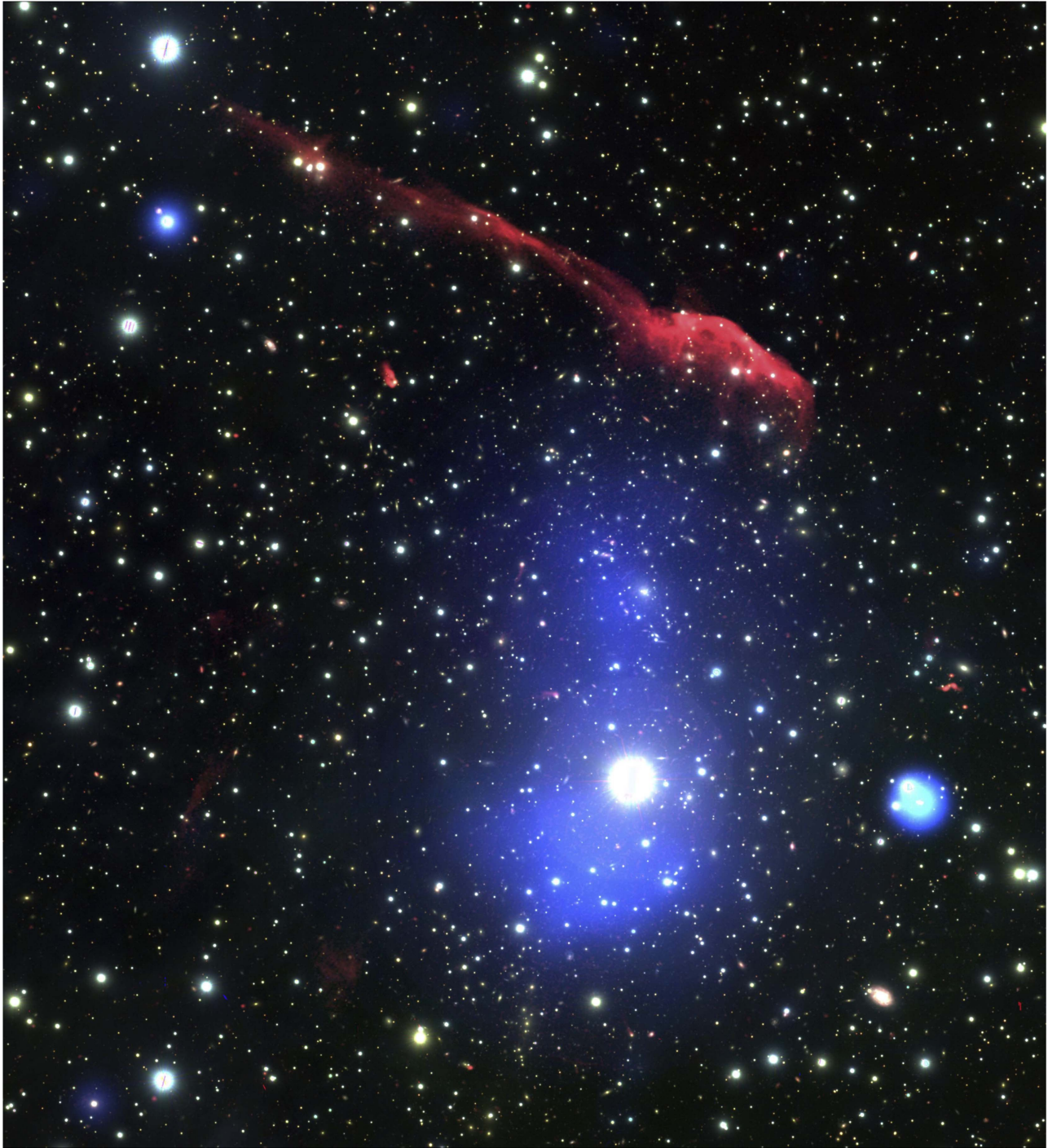


Figure 6. Radio, X-ray, and optical overlay of cluster 1RXS J0603.3+4214. The intensity in red shows the radio emission observed with VLA at a central frequency of 1.5 GHz. The VLA image properties are given in Table 2, IM3. The intensity in blue shows *Chandra* X-ray emission in the 0.5–2.0 keV band, and in the background is the color composite optical image created using Subaru data with g, r, and i intensities represented in blue, green, and red, respectively.

may find even flatter spectral indices. However, the origin of this resolution dependent flattening might be more complex, as we will report in Section 5.3.

The radio brightness distribution across the northern edge of the Toothbrush, with distance increasing from east to west, is displayed in Figure 9. It is evident that the relic brightness is not uniform across its extension.

The comparison of the spectral index and brightness distribution along the northern edge of the Toothbrush, from

east to west (same region where we extracted spectral indices), reveals that there is a correlation between these two (i.e., brighter regions tends to be flatter). Variations on the order of 0.2 in the spectral index are seen in the brightest regions, like in the brush. For a curved electron energy distribution, an increase in the magnetic field strength will increase the emissivity, which brightens the emission and flattens the spectrum (Ellison & Reynolds 1991). We carried out a Spearman’s rank correlation test to check the possible correlation between

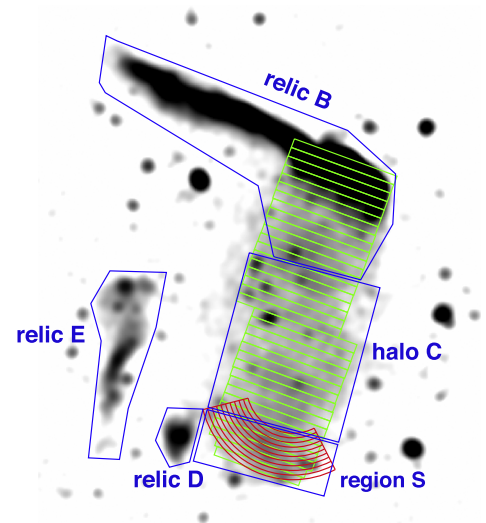
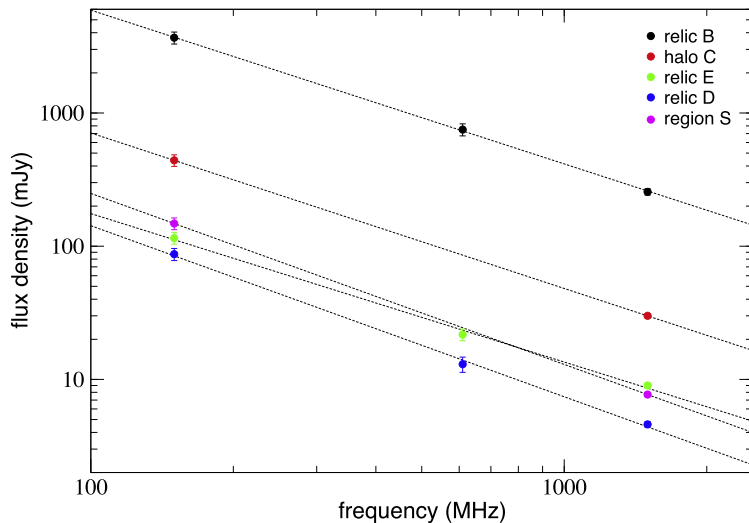


Figure 7. Left: integrated spectra of the radio sources B, C, E, and D and region S for 150 MHz, 610 MHz, and 1.5 GHz. Dashed lines are fitted straight power-laws with indices given in Table 4. The radio spectrum of relics B, D, and E are well described by a single power-law spectrum. The radio halo and region S is not detected in the GMRT 610 MHz image. Right: VLA 16'' resolution image depicting the regions where the integrated flux densities were measured. The green boxes have a width of 16'' and were used to extract the spectral index across the halo.

spectral index and brightness. From this test, we find that the p -value is less than 0.05, which indicates that correlation is statistically significant.

The spectral index map for fainter relics is shown in Figure 10. To create the spectral index map for relic E and D, we convolve the VLA and LOFAR image to a common resolution of $11'' \times 11''$.

The spectral indices in relic E range from -0.70 to -1.50 . For some regions of relic E, our high resolution spectral index map reveals a relatively flat spectral index of about -0.70 ± 0.10 ; see Figure 10. We investigate regions showing flatter spectral index and searched for compact radio sources with optical counterparts. From the radio-optical overlay (Figure 6), it is clear that the brightest regions (EA, EB, and EC), showing a flat spectral index, namely $\alpha = -0.70$, do not show any optical counterparts.

Relics are expected to show a spectral index gradient, as the Toothbrush or Sausage-relic (van Weeren et al. 2010, 2012a, 2016; Hoang et al. 2017). We do not find a significant spectral index gradient toward the cluster center (i.e., from east to west) for relic E.

For relic D we confirm the southwest spectral index steepening, varying from -0.85 to -1.70 , as reported by van Weeren et al. (2016). They found the spectral index for relic D is in the range of -0.90 to -1.40 . It is interesting to see that spectrum flattens from south to west while the bright region of relic D (cone) is at the west, which shows a relatively steeper spectrum.

Relics E and D show a quite unusual morphology; however, we do not find any connection to a nearby radio galaxy. Given the relatively small size and peculiar morphology of relic D, we speculate it could trace revised fossil radio plasma, possibly re-accelerated by a merger induced shock. A similar scenario could also hold for relic E. It should be noted that due to the rather flat spectral index along the 1.1 Mpc extent of relic E, the source cannot simply be an old radio tail, as spectral ageing would have resulted in a much steeper spectral index along the tail extent.

5.3. The Ridge

We can study the brush region with a resolution as good as about $1''$ due to its high surface brightness. Figure 3 reveals its complex structure. A remarkable feature is the bright ridge with a relatively clear boundary. At the most narrow region, the ridge has a width of about 25 kpc. This raises the question about its origin. The high surface brightness across the ridge could be a projection effect of a shock front parallel to the line of sight. Alternatively, the ridge could originate from enhanced synchrotron emission due to a magnetic filament.

We extract the surface brightness profiles from VLA, GMRT, and LOFAR data in a region where the ridge is particularly narrow; see Figure 9, right panel. The resultant profiles across the ridge are shown in Figure 11. Evidently, the width and the position of the ridge depend on the observing frequency. The peak surface brightness shifts by about 7 kpc between the VLA and the LOFAR frequencies. The shift is consistent with an intrinsic profile that gets wider at lower frequencies. Such a behavior is expected if the ridge is caused by a shock front seen edge-on and its downstream width is determined by CRe cooling. For a shock front seen perfectly edge-on, the downstream width scales according to $1/\sqrt{\nu_{\text{obs}}}$, where ν_{obs} is the observing frequency (Hoeft & Brüggen 2007).

The smallest downstream width has been reported so far for the Sausage-relic, namely 55 kpc at 610 MHz (van Weeren et al. 2010). Taking into account that the width scales with the observing frequency, as provided previously, the ridge is still significantly narrower than the Sausage-relic. The narrowness of the ridge restricts the magnetic field strengths in the downstream area. To quantify this, we compute the downstream profile $S_{\nu}(x)$ according to Hoeft and Brüggen (2007). We use a slightly more elaborate computation. For instance, we now include a pitch angle average representing a fast isotropization according to the so-called Jaffe-Perola model (Jaffe & Perola 1973). We adopt a power-law electron injection spectrum. Assuming DSA in the test-particle regime and a hydrodynamical shock, we can relate the Mach number, the speed of the downstream plasma relative to the shock front, and the spectral index of the CRe distribution (Blandford &

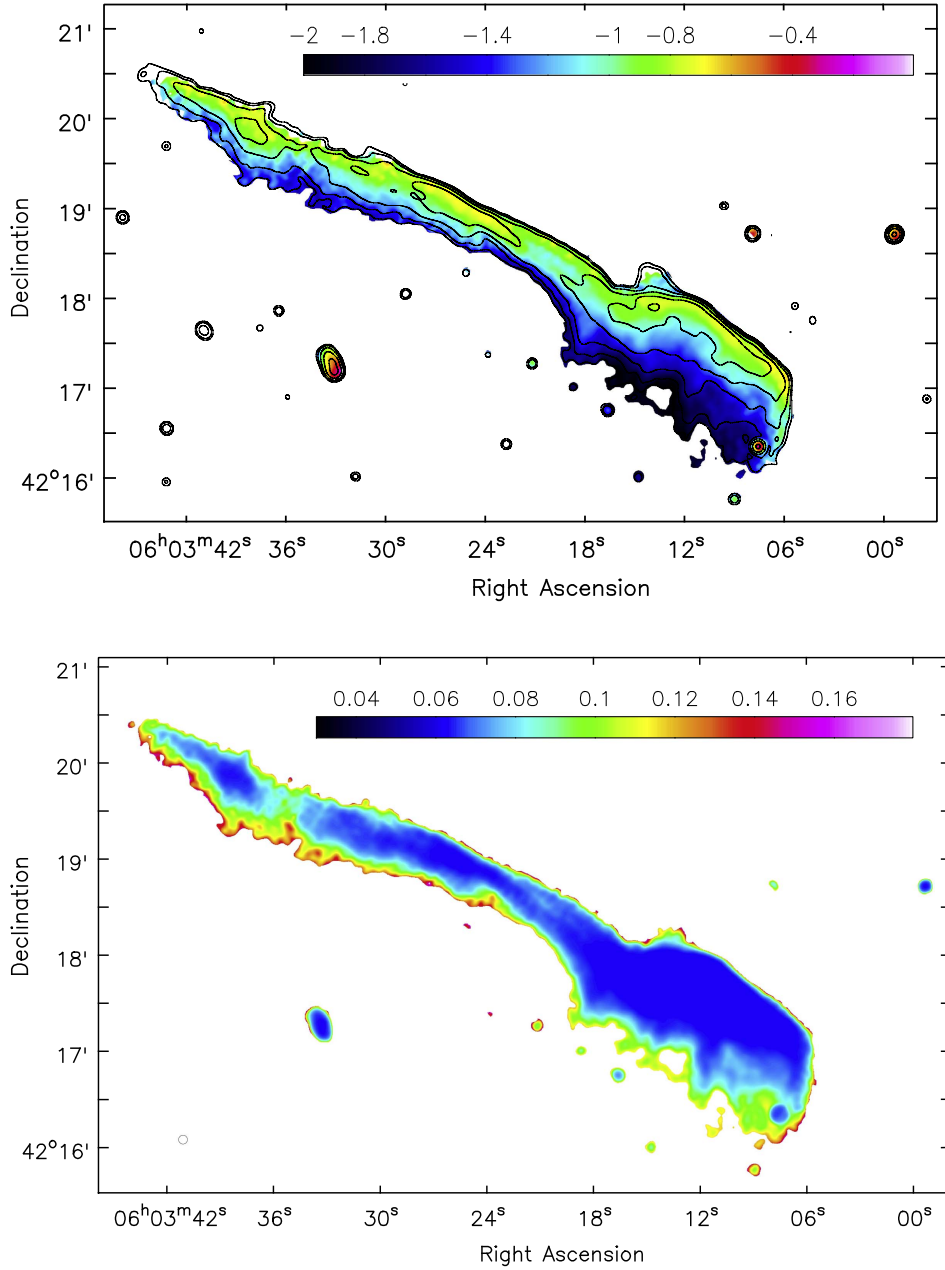


Figure 8. Top: spectral index map of the Toothbrush between 150 MHz and 1.5 GHz at $5''/5$ resolution, overlaid with the VLA contours. The image properties are given in Table 2, IM6. Contours show the VLA flux density distribution. The contour levels are drawn at $[1, 2, 4, 8, \dots] \times 4.5 \sigma_{\text{rms}}$. The color bar shows spectral index α from -0.2 to -0.4 . Bottom: corresponding spectral index uncertainty map.

Eichler 1987). Figure 12 shows the downstream profiles for three different magnetic field strengths. The Mach number has been chosen to approximately match the peak flux ratio between the VLA and LOFAR profiles. It is evident that a $3 \mu\text{G}$ profile decreases too slowly (i.e., it is not consistent with the narrowness of the ridge). With a significantly higher or lower magnetic field strength, the downstream profile would roughly match the narrow ridge.

Another remarkable feature of the ridge is its northern edge. In the highest resolution VLA profile, it has a half width half maximum (HWHM) of about 11.8 kpc; see Figure 12. This is a quite sharp edge; still the HWHM is evidently larger than the beam size, namely $1''/5$ corresponding to 5.5 kpc. Therefore, the intrinsic surface brightness profile must show a slope to the north instead of a sharp edge. If the slope is caused by

diffusion, we can roughly estimate the diffusion constant. Assuming that the shock front propagates with a speed of the order of 1000 km s^{-1} , it would sweep up a 5 kpc upstream region within 5 Myr. Hence, if diffusion causes the slope, it must distribute the CRE in ~ 5 Myr to a distance of ~ 5 kpc upstream. This corresponds to a diffusion constant of $D_{\text{diff}} \approx 1.5 \times 10^{30} \text{ cm}^2 \text{ s}^{-1}$. The derived value is about one order of magnitude larger than the diffusion constant of CRE transport in the halo of NGC 7462, found by Heesen et al. (2016), by assuming that CRE visible in synchrotron emission have energies of a few GeV. However, the value roughly corresponds to the maximum turbulent diffusion found by Vazza et al. (2012). Hence, forming the slope by diffusion would require a significantly more efficient diffusive CRE transport than expected. However, the provided calculation

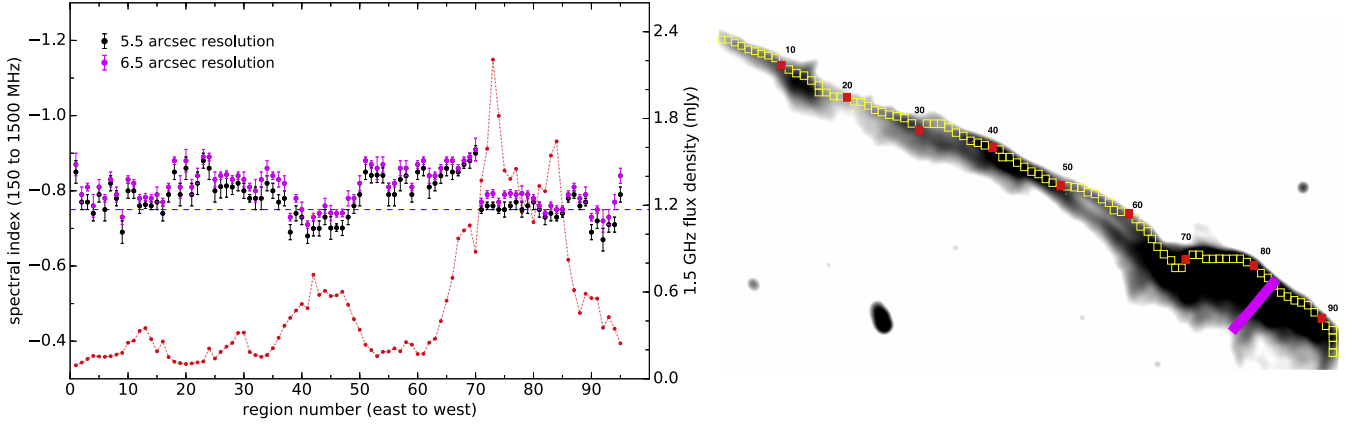


Figure 9. Left: extracted spectral index between 150 and 1500 MHz across relic B1, from north to south, with the distance increasing from east to west. The black dots show the spectral index distribution at a resolution of $5''.5$ while the magenta at $6''.5$ resolution. The dashed blue horizontal line indicates the average spectral index of $\alpha = -0.75 \pm 0.05$ at the ridge. A shift in the spectral indices is clearly visible across the entire relic caused by lowering the resolution. The red dots trace the VLA 1.5 GHz flux density along the relic, corresponding to the spectral indices shown with the magenta color, revealing a correlation between the brightness and the spectral index. Systematic uncertainties in the flux-scale were included in the error bars. Right: box distribution across relic B overlaid on the VLA total intensity map at $5''.5$ resolution. The width of the boxes used to extract the indices is $5''.5$. The magenta colored region is used to study the ridge. To obtain the flux densities, we create small rectangular boxes, inside the magenta region, with a width of $0''.7$ corresponding to 2.5 kpc. The total length of the magenta region is about 164 kpc.

assumes that the shock surface is completely flat and perfectly aligned along the line of sight.

We suggest that the ridge is formed by projection of a shock front along the line of sight. The possible scenario is sketched in Figure 13. The shock front is curved, but still a large fraction of the front is rather parallel to the line of sight and causes the large surface brightness enhancement of the ridge. Very likely the magnetic field strength in the ICM is not homogeneous. Hence, for such a large shock front seen in projection, it is plausible to assume that the magnetic field strength, which determines the downstream width, varies significantly along the line of sight. The observed profile is an average

$$S_{\nu,av}(x) \propto \int dB h(B) S_{\nu}(x; B), \quad (6)$$

where $S_{\nu}(x; B)$ is the profile for one particular magnetic field strength and $h(B)$ encodes the fractional abundance of the field strength B along the line of sight. We assume that the shock front is much more extended along the line of sight than the downstream width. Hence, we expect that the magnetic field strength may vary significantly. To model this, we adopt a log-normal distribution as a toy model for a complex magnetic field distribution in the downstream region

$$h(B; B_0, \sigma) dB = \frac{1}{\sqrt{2\pi}\sigma B} \exp\left\{-\frac{\ln(B/B_0)}{2\sigma^2}\right\} dB, \quad (7)$$

with a width σ and central field strength B_0 .

The projection of a curved shock front (see Figure 13) also implies that injection not only takes place at the outermost edge but also at what appears to be downstream of the outermost edge. Therefore, the observed surface brightness distribution is the sum of profiles shifted according to the projection and averaged according to the magnetic field distribution. We model this by introducing an injection distribution $W(x)$. Our toy model becomes

$$S_{\nu,con}(x; B_0, \sigma, W) = \int dx' W(x') S_{\nu,av}(x - x'). \quad (8)$$

We demand here that the sum of the surface brightnesses in all regions i matches the VLA observation

$$\sum_i S_{\nu_0,i} \stackrel{!}{=} \sum_i S_{\nu_0,con}^{\text{mod}}(x_i; B_0, \sigma, W), \quad (9)$$

where ν_0 indicates the VLA observing frequency. This procedure determines the normalization of the GMRT and LOFAR profiles. This means we do model the spectral index and curvature but we do not model the absolute luminosity.

We do not know the actual shape of the shock front. Therefore, we estimate the injection distribution from the observed profiles. To this end, we measure the difference between model and observed profiles via

$$D^2 = \frac{1}{S_{\max,k}^2} \sum_k \frac{1}{N_k} \sum_i (S_{\nu_k,i}^{\text{obs}} - S_{\nu_k,con}^{\text{mod}}(x_i; B_0, \sigma, W))^2, \quad (10)$$

where $S_{\nu_k,i}^{\text{obs}}$ denotes the measured surface brightness at frequency ν_k and position x_i , and $S_{\nu_k,i}^{\text{mod}}$ the surface brightness at x_i according to our model. We search for the “optimal” injection distribution $W(x)$ using a small routine that varies the injection distribution $W(x)$ by adding and subtracting Gaussians with a random position, width, and amplitude. Modifications that lower D^2 are accepted; others are rejected. To improve the stability of the optimization scheme, we compute several injection distributions with lower D^2 and take the average before proceeding with the optimization. Figure 14 shows the initial guess, the optimized distribution, and the resulting surface brightness distribution for two different magnetic field models. For a homogeneous magnetic field, model A, a clear mismatch for the LOFAR profile is evident, despite the fact that the VLA and GMRT match reasonably well. For a broad distribution of magnetic field strengths, model B, we obtain a reasonable match for all observing frequencies.

The $W(x)$ that best matches the observation shows several interesting features. First of all, the region where $W(x)$ is high corresponds to the northern slope of the ridge. Therefore, the HWHM found in the slope is determined by the curvature of the shock front or its “mis-alignment” to the line of sight. As a consequence, CRE diffusion must be much less efficient than

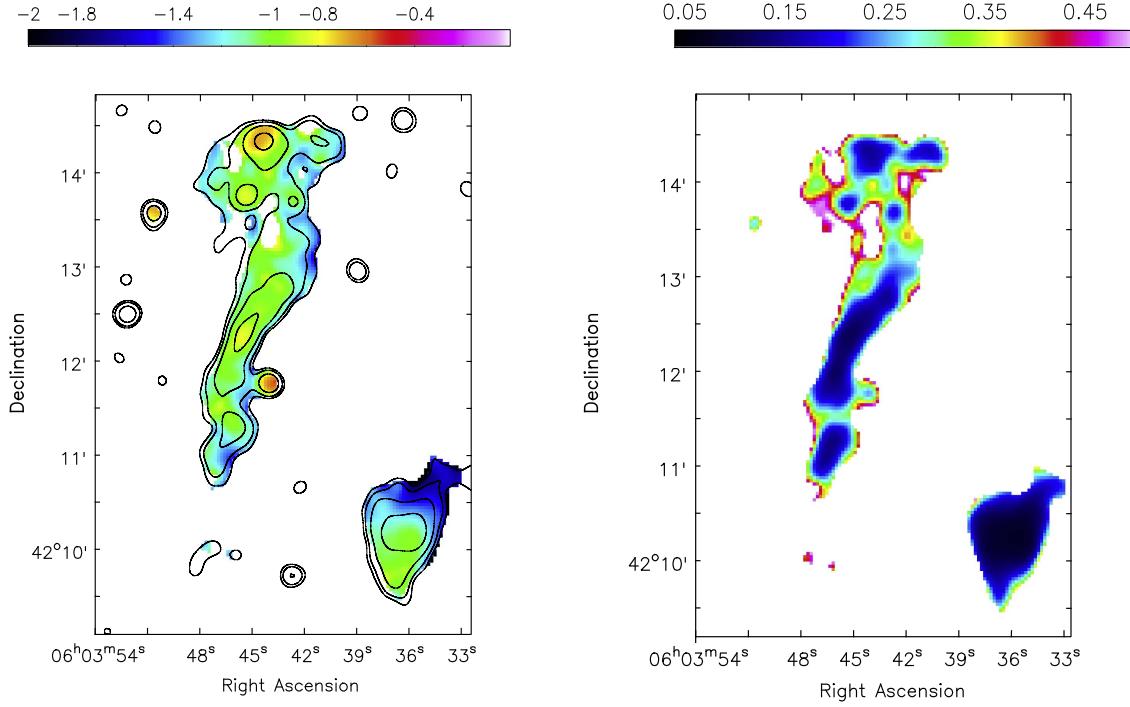


Figure 10. Left: spectral index map for the relics E and D between 150 and 1500 MHz at $11.0''$ resolution. The image properties are given in Table 2, IM12. Contours show the VLA flux density distribution. The contour levels are from the VLA and drawn at $[1, 2, 4, 8, \dots] \times 4.5\sigma_{\text{rms}}$. The color bar shows spectral index α from -2.2 to -0.4 . Right: corresponding spectral index uncertainty map.

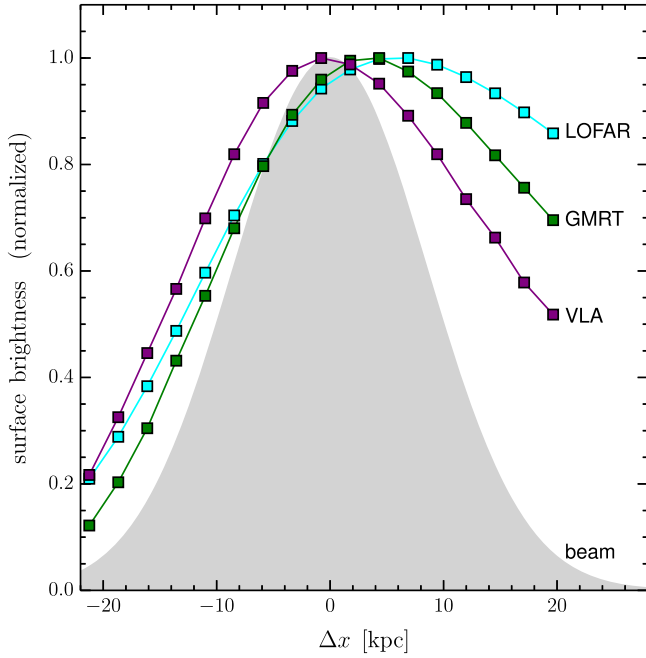


Figure 11. Surface brightness profiles measured in the magenta regions shown in Figure 9, right panel, for the VLA, the GMRT, and the LOFAR observations, depicted with purple, green, and cyan, respectively. To measure these profiles, all observations have been imaged with the same restoring beam width, namely $5''/5''$, indicated by the gray area. For all three observations, the extracted profiles are normalized by the peak flux. From VLA to LOFAR, the peak shifts to the right and gets wider.

estimated previously. Moreover, we find that there are strong variations of $W(x)$ along the x -axis. For instance, we clearly see a double peak in the ridge region, which is in accord with the

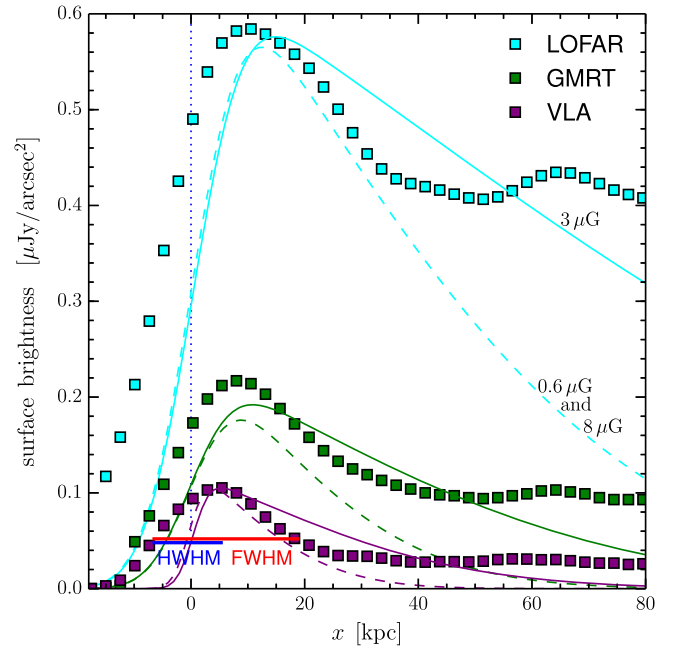


Figure 12. Surface brightness profiles (squares) measured in the magenta regions shown in Figure 9, right panel, and model profiles assuming a single location of CRE injection at $x = 0$ plus subsequent cooling. The resolution of the VLA, GMRT, and LOFAR images are $1''/5$, $3''/8$, and $4''/4$, respectively. Model profiles are smoothed according to the resolution in the observations and normalized to match the peak surface brightness in the VLA profile. A Mach number of $\mathcal{M} = 3.1$ is assumed to match the LOFAR peak surface brightness. Three magnetic field strengths have been assumed for the downstream CRE cooling—that is, $3 \mu\text{G}$ (solid line), 6 and $8 \mu\text{G}$ (dashed line). A magnetic field of $3 \mu\text{G}$ would cause a too wide downstream region. The VLA profile shows a rising slope with a half width half maximum of $\text{HWHM} = 11.8 \text{ kpc}$ and width of $\text{FWHM} = 25.3 \text{ kpc}$.

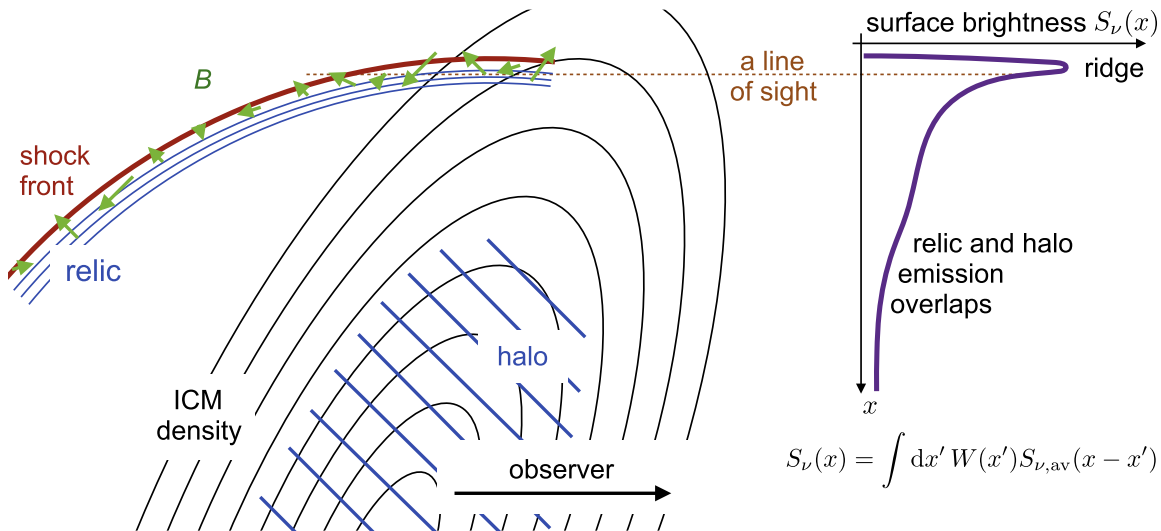


Figure 13. Sketch of the proposed shock geometry. The shock front extends behind the cluster. However, the strong depolarization suggests that the emission lies behind the ICM (Kierdorf et al. 2016). With red we indicate the shock front where electrons are accelerated and injected as CRe into the ICM. The green arrows represent a tangled magnetic field in the ICM with varying field strength. The single location of CRe injection at $x = 0$ is shown with a dotted line. The function $W(x)$ encodes the pile-up of injection at position x due to projection effects.

apparent branching of the ridge to the west; see Figure 14. The branching may reflect a complex structure of the actual shock surface. There are also areas where $W(x)$ is close to zero, indicating that the injection varies significantly across the shock front. This may suggest that the small filaments, “bristles,” also reflect variations of the injection across the shock front or just variations of the angle between the line of sight and the magnetic field orientation. If the magnetic field is aligned with the line of sight, the synchrotron emissivity vanishes.

To estimate which parameters best reproduce the observed profile, we raster the B_0 - σ parameter space; see Figure 15. Several aspects become evident: magnetic field distributions with $B_0 \gtrsim 5 \mu\text{G}$ do not provide a good match between observed and modeled profiles, irrespective of a narrow or broad distribution of field strengths. For $B_0 \lesssim 3 \mu\text{G}$, there is always a combination of B_0 and σ , which provides a good match, where σ becomes larger for lower B_0 . This may reflect that always some regions are needed which show a wide downstream profile, since for about $3 \mu\text{G}$ the downstream profile is widest. Comparing different Mach numbers, we find that $\mathcal{M} = 3.75$ provides the best match, while for $\mathcal{M} = 3.5$ and 4.0 the minimum difference D^2 found in the B_0 - σ parameter space gets larger. The Mach number preferred in the model is even higher than that obtained from the flattest region in the spectral index map but agrees with the one obtained from the overall spectrum. In spectral index maps, projection effects and convolution with the beam smear out the profiles and prevent actual measurement of the injection spectral index. Finally, best matches are achieved for a considerably broad magnetic field distribution, namely for $\sigma \gtrsim 0.5$. No uniform magnetic field matches the observations as well as a broad magnetic field distribution.

To summarize, several interesting insights are obtained from the simple toy model. First, one has to be careful when interpreting an observed spectral index as the injection spectrum. In a case of $W(x)$ as wide or wider than the downstream CRe cooling width, projection effects may steepen the observed spectral index (i.e., the spectral index can only provide a lower limit for the actual injection spectral index, as shown for the profile investigated here and as found in

Section 5.2). For instance, the observed spectral index at the ridge is $\alpha_{\text{inj}} \approx -0.70$, but the best match of the profiles is found for a Mach number corresponding to an injection spectral index $\alpha_{\text{inj}} = -0.65$. Moreover, our toy model suggests that broad magnetic field distributions are favored with width $\sigma \gtrsim 0.5$ and a central field strength $B_0 \lesssim 3 \mu\text{G}$.

5.4. Mach Numbers Derived from Integrated Spectra, Model and Spectral Index Map

Using VLA data, together with existing LOFAR and GMRT data, we measured an integrated spectral index of $\alpha = -1.15 \pm 0.02$, suggesting a Mach number of $\mathcal{M} = 3.78_{-0.2}^{+0.3}$; see Table 4.

Our model resulted in a best match for Mach number of $\mathcal{M} = 3.75$ for the northern shock. The integrated spectrum and modeling give consistent Mach numbers.

Another way to obtain a Mach number using radio observations is to measure the injection spectral index directly from the high resolution spectral index maps. From the spectral index map, we find that the flattest spectral index at the northern shock front is about -0.70 . This injection corresponds to a Mach number of $\mathcal{M} = 3.3_{-0.3}^{+0.4}$. Due to the projection effects discussed in Section 5.3, the measured injection index does not necessarily indicate the actual injection spectrum. Hence, the Mach number obtained from the radio spectral index map is a lower limit.

The deep *Chandra* observations of 1RXS J0603.3+4214 revealed a weak shock of Mach number $\mathcal{M}_{\text{X-ray}} \approx 1.2$ at the northern edge of the Toothbrush (van Weeren et al. 2016). Clearly the derived radio and X-ray Mach numbers differ significantly. The recent polarization study of the Toothbrush by Kierdorf et al. (2016) suggests that the relic lies behind the cluster. We argue that the X-ray observation underestimates the strength of the shock, since unshocked ICM along the line of sight lowers the measured surface brightness and temperature jumps. We suggest that the shock in the densest region is rather weak; see Figure 13. Finally, the ridge branching may indicate that the geometry of the shock front is complex, and hence the transition might be significantly smeared out.

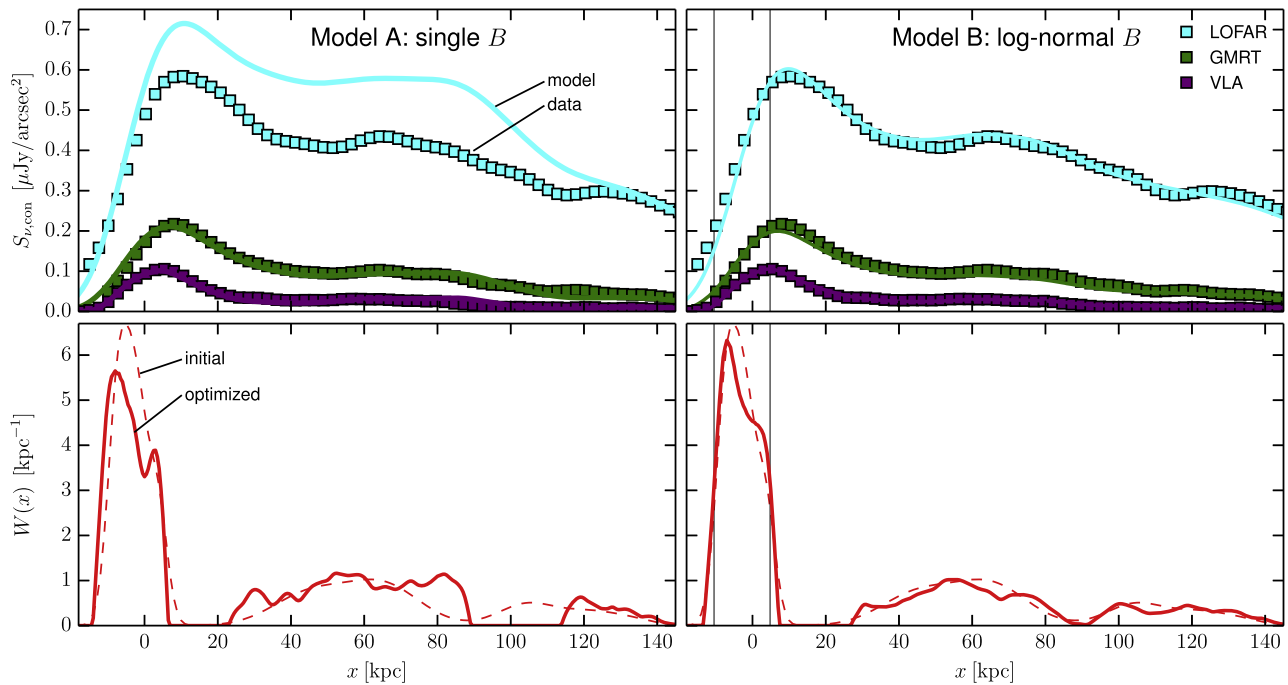


Figure 14. Surface brightness (top panels) and injection distributions $W(x)$ (bottom panels) for two different models. Left: a homogeneous magnetic field model; $\mathcal{M} = 3.0$, $B_0 = 6.81 \mu\text{G}$, and $\sigma = 0.001$ (Model A). The lower panel shows the result of the injection distribution optimization, the dashed line shows the initial guess, and the solid line shows the final optimization. Right: a broad distribution of magnetic field strength; $\mathcal{M} = 3.75$, $B_0 = 0.46 \mu\text{G}$, and $\sigma = 1.3$ (Model B). Model B evidently matches the observed profiles better. The two vertical lines in the right panel indicate that the northern rising slope of the ridge corresponds to an extended region where $W(x)$ is high.

5.5. Analysis of the Halo

X-ray observations of the cluster 1RXS J0603.3+4214 showed that the ICM is dominated by two components (Ogrea et al. 2013; van Weeren et al. 2016). The southern component is brighter than the northern one. The high resolution *Chandra* image revealed the presence of a cold front at the southern edge of a triangular “bullet-like” structure (van Weeren et al. 2016).

In Figure 16, we compare the X-ray morphology of the cluster to that of the radio emission. The X-ray and the radio morphology are strikingly similar, indicating a connection between the thermal gas and relativistic plasma in this system. The emission from the radio halo extends over the whole region of detected X-ray emission. It is worth emphasizing that the X-ray surface brightness enhancement between the two sub-clusters and the radio surface brightness in the same region follow each other. However, the radio emission extends further to the south where the X-ray emission is fainter, “region S,” shown in Figure 5. It is noteworthy that van Weeren et al. (2016) recently reported the presence of a shock front ($\mathcal{M} = 1.39 \pm 0.06$ via the density jump) at the southern edge of region S, shown with a yellow line in Figure 16. The southern boundary of region S is edge sharpened and aligns with the southern shock. A similar positioning is observed in others clusters also—for example, the Bullet cluster (Shimwell et al. 2014), A754 (Macario et al. 2011), A2744 (Owers et al. 2011; Pearce et al. 2017), A520 (Vacca et al. 2014), and the Coma cluster (Uchida et al. 2016).

In order to examine and compare the X-ray and radio emission going along the line from B1 to region S with distance increasing from north to south, we calculate the average brightness along the major axis of the radio halo. As mentioned in Section 4.2, there are 32 discrete sources embedded within the halo. It is important to first subtract discrete unrelated

sources. After subtracting strong sources from the uv-data, we measure the surface brightness in the green regions as indicated in Figure 7, right panel. We smoothed the X-ray image with a Gaussian to a FWHM of $16''$ (i.e., similar to the restoring beam of our VLA map). The resultant 1.5 GHz VLA and *Chandra* profile is shown in Figure 17. The X-ray and radio profile clearly show two sub-cluster components. We find that the center of the northern and the southern sub-cluster of the radio emission are coincident with the X-ray and there is no offset. However, within the halo there is a region where the radio brightness is relatively lower than the X-ray. We note that the halo region where the radio brightness is lower is dominated by strong discrete sources. We subtracted strong sources, but the source subtraction leaves zero flux at their location, which might be a possible reason for the observed low radio brightness. The radio profile also reveals a region of prominent enhanced emission that does not correlate with the X-ray, exactly between the cold front and the southern shock front.

The comparison of the X-ray and the radio brightness profile, as shown in Figure 17, suggests that the emission in region S has a different origin than the halo. A cluster undergoing a merger drives shocks and generates turbulence throughout the ICM, providing potential acceleration sites for relativistic particles responsible for radio halos (Feretti et al. 2012; Brunetti & Jones 2014). As there is a shock detected at the southern edge of region S, this region could be related to that shock front. We will investigate this possibility in Section 5.5.1.

In several clusters hosting a giant radio halo, a radio to X-ray spatial correlation has been observed—for example, in Abell 2319, Abell 2163, Abell 2744, Abell 520, Abell 2255, and the Coma (Feretti et al. 2001; Govoni et al. 2001a, 2001b; Venturi et al. 2013; Vacca et al. 2014). To investigate the

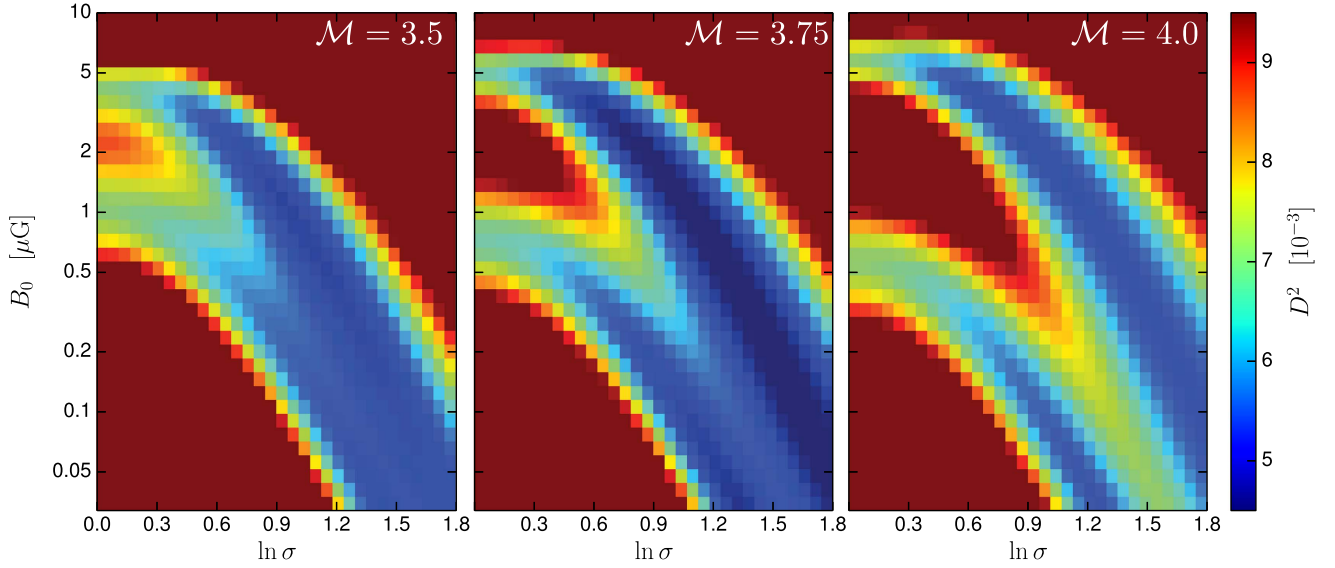


Figure 15. Difference D^2 between model and observed profiles for different log-normal models for three different Mach numbers. For each B_0 - σ parameter combination in each panel, the injection distribution $W(x)$ has been optimized and the resulting minimum D^2 determined. From left to right, the model Mach numbers are $\mathcal{M} = 3.5, 3.75$, and 4.0 . Dark blue areas indicate where the difference between model and observed profiles is minimal. The Mach number $\mathcal{M} = 3.5$ provides the best match.

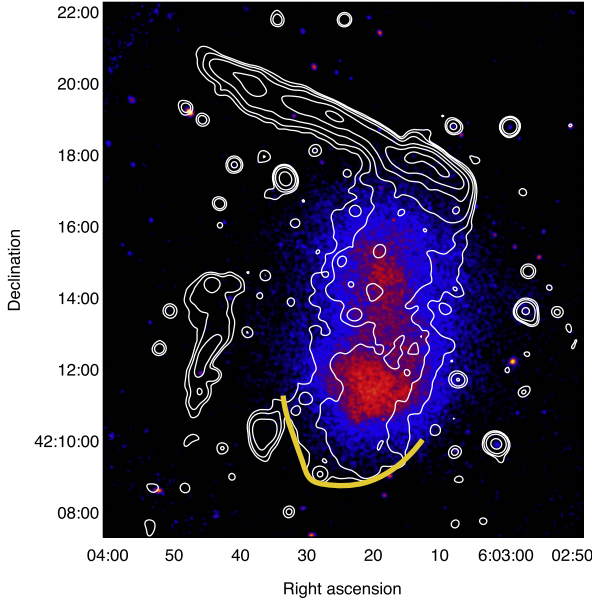


Figure 16. VLA 1–2 GHz radio contours at the resolution of $15''$ superposed on the *Chandra* X-ray image (0.5–2 keV band), smoothed to FWHM of $4''$ (van Weeren et al. 2016). The VLA image properties are given in Table 2, IM13. Contour levels are drawn at $[1, 2, 4, 8, \dots] \times 4.5 \sigma_{\text{rms}}$, where $\sigma_{\text{rms}} = 16 \mu\text{Jy beam}^{-1}$. Negative $-4.5 \sigma_{\text{rms}}$ contours are shown with dotted lines. The yellow line shows the location of the southern shock front detected in *Chandra* observations (van Weeren et al. 2016).

possible presence of a radio to X-ray correlation, we performed a quantitative point-to-point comparison of the radio and X-ray brightness. The brightness distribution was constructed using a square grid covering the region where the radio halo emission is higher than the 3σ level. The grid cell size is equal to $30''$, corresponding to a physical size of about 109 kpc. We exclude regions where there is a point source. The plot of the radio versus X-ray brightness, excluding region S, is shown in Figure 18. The radio brightness correlates well with the X-ray brightness; a higher X-ray brightness is associated with a

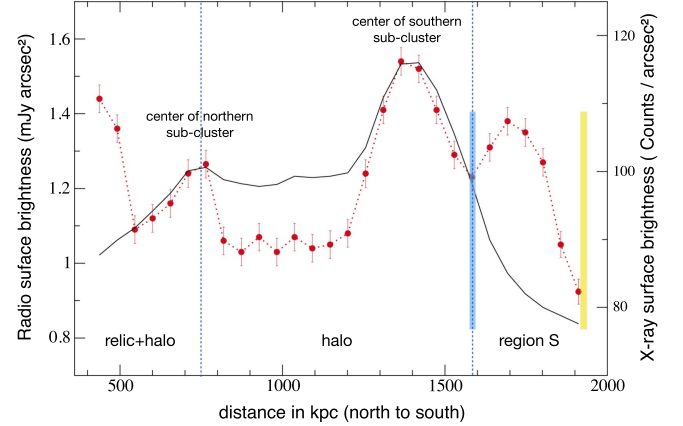


Figure 17. Radio and X-ray surface brightness profiles along the major axis of the radio halo. The 1.5 GHz VLA brightness profile at a resolution of $16''$ is shown with red dots, while the *Chandra* X-ray profile convolved with the same resolution is shown with a black solid line. The VLA image properties are given in Table 2, IM14. The vertical blue and yellow line indicate the location of the cold front and the southern shock front.

higher radio brightness. The data was fitted with a power-law of the type

$$I_{\text{radio}} \propto I_{\text{X-ray}}^b, \quad (11)$$

where the radio brightness I_{radio} is expressed in $\mu\text{Jy beam}^{-1}$ and the X-ray brightness $I_{\text{X-ray}}$ in $\text{mCounts s}^{-1}\text{arcsec}^{-2}$. We obtained a slope of $b = 1.25 \pm 0.16$. This is more or less consistent (within 2σ) with the radio surface brightness proportional to the X-ray surface brightness, as found for other giant radio halos (Govoni et al. 2001a, 2001b).

The radio and the X-ray brightness distribution across region S (i.e., the region between the cold front and the southern shock front) is indicated by red dots in Figure 18. We do not include source W (see Figure 1 panel (c) for labeling, as this region consist of two compact sources). The region S is evidently distinct and does not appear to be connected with the rest of the halo.

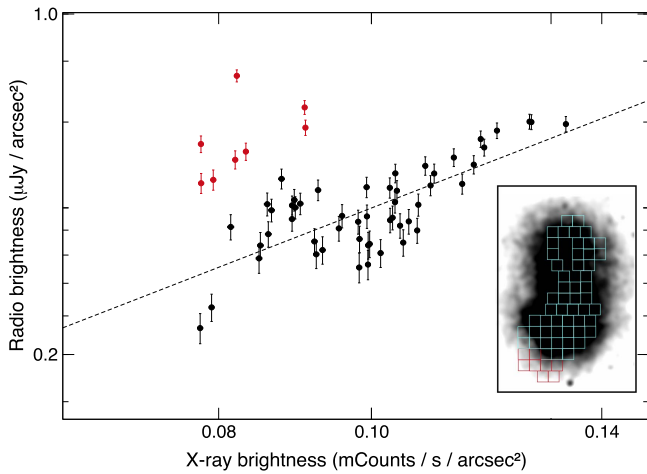


Figure 18. $I_{\text{radio}}-I_{\text{X-ray}}$ relation of the 1RXS J0603.3+4214 cluster. The error bars represent the rms of the brightness distribution within each cell. The power-law fit is indicated by a dashed line. Red and cyan boxes, overlaid on the *Chandra* X-ray image, show the regions where the radio and X-ray surface brightness were extracted. We exclude regions where there is a point source. The surface brightness extracted in cyan cell are indicated by black dots. The red dots are extracted across the southernmost part of the radio halo (i.e., the region between the cold front and the southern shock front, shown as red regions). As discussed in Section 5.5, the southern part of the radio halo may have a different origin than the rest of the halo.

5.5.1. Spectral Indices

The radio halo spectral index maps provide useful information on their origin and connection with the merger processes. The spectral index distribution is also important to test predictions of different models for the electron energy distribution. For example, a systematic variation of the radio halo spectral index with distance from the cluster center is predicted by the re-acceleration process modeled in Brunetti et al. (2001).

The deep VLA images allow us to create spectral index maps for the radio halo at higher resolution and with high accuracy. To make spectral index maps of the halo between 150 MHz and 1.5 GHz, we employed the same weighting and uv cut, as mentioned in Section 5.2. We convolve the LOFAR and VLA images to a common resolution of $16''$. We did not subtract the extended or point-like discrete sources to create the spectral index map, but these sources can be well identified from the halo emission. Pixels with flux densities below $5\sigma_{\text{rms}}$ were blanked. Figure 19 shows the spectral index image of the radio halo overlaid with the VLA contours.

The spectral index across the entire halo varies between -2.0 and -0.95 and shows a slight gradient from north to south. We do not find a region with somewhat steeper spectrum (see Figure 19) at the eastern part of the halo, toward relic E, as found by van Weeren et al. (2016). As argued before in Section 5.1, there is a region where, at 1.5 GHz, the halo dominates the surface brightness and at 150 MHz the relic dominates. Moreover, the southern part of the halo (region S in Figure 5) may have a different origin than the central part of the halo.

The spectral index distribution from north to south, covering the B1 region of the Toothbrush and the entire radio halo, is shown in Figure 20. Moving from B1 toward region S, the spectral index varies mainly between -0.90 and -1.90 . The spectrum first steepens in the post-shock regions to -1.90 (360 kpc). After this, the spectrum gradually flattens over a distance of about 400 kpc (relic+halo region). For a distance of

800 kpc, the spectrum remains relatively constant with a mean of -1.16 (central halo region) and steepens again to the south (region S).

The spectral index of the Toothbrush shows a strong steepening in the downstream areas, while in the relic+halo region, the spectrum flattens progressively. It has been speculated that this spectral behavior indicates a possible connection between shock and turbulence (van Weeren et al. 2016).

We note that at 150 MHz (see Figure 5), the brush region appears wider with several streams coming out of it, extending from the north to the south. The surface brightness across these streams is very high, and the whole emission in this region is mainly dominated by the relic. In contrast, at 1.5 GHz the same region is dominated by the halo emission. Therefore, the strong steepening and gradual flattening of the spectrum in the “relic+halo” region could be due to the projection of the halo and the relic emission. It has been suggested that the relic lies behind the cluster (Kierdorf et al. 2016). Hence the relic and halo could be separated physically, but in projection, one finds the gradual steepening and flattening.

The spectral index across the central part of the halo, excluding the “relic+halo” and region S, is in the range of $-0.95 \leq \alpha \leq -1.25$. To estimate the measurement uncertainties, we followed Cassano et al. (2013). We find a raw scatter of 0.05 from the mean spectral index, excluding pixels which are point sources. For the radio halo in 1RXS J0603.3+4214, the spectral index uncertainties are much smaller than those of the radio halo in Abell 665, Abell 2163, Abell 520, Abell 3562, 1E 0657-55.8, and Abell 2744 (Feretti et al. 2004; Giacintucci et al. 2005; Orrú et al. 2007; Shimwell et al. 2014; Vacca et al. 2014).

For the radio halo in Abell 2744, a point-to-point correlation has been observed for the first time, indicating that halo regions with flat spectra correspond to regions with hotter temperatures (Orrú et al. 2007). Such a trend is expected, since a fraction of the gravitational energy which is dissipated during cluster merger events in heating thermal plasma is converted into re-acceleration of highly relativistic particles and amplification of the ICM magnetic field. However, a recent study of the same radio halo by Pearce et al. (2017) reveals that there is no statistically significant correlation. For the present radio halo, the point-to-point comparison of our high resolution spectral index map to that of the temperature map does not show any correlation. Hence we confirm that there is no strong correlation between the radio spectral index and X-ray temperature, reported by van Weeren et al. (2016). However, the southernmost part of the radio halo (i.e., Region S) is characterized by a hot ICM, namely $T = 14-15$ keV (Figure 11 of van Weeren et al. 2016).

To study the spectral distribution across the southernmost region of the halo (i.e., region S), we extract the spectral indices in regions shown with red annuli in Figure 7, right panel. The resultant distribution is shown in Figure 21. The spectral index distribution in region S shows a clear spectral index gradient, namely $\alpha = -1.20$ to -1.35 , from north to south.

The southern boundary of the radio halo is relatively well defined and coincides with the southern shock front reported by van Weeren et al. (2016). This part of radio halo was speculated to be a fainter relic (van Weeren et al. 2012a), but a uniform spectral index distribution disfavored this scenario. Our spectral index map reveals a spectral index gradient across

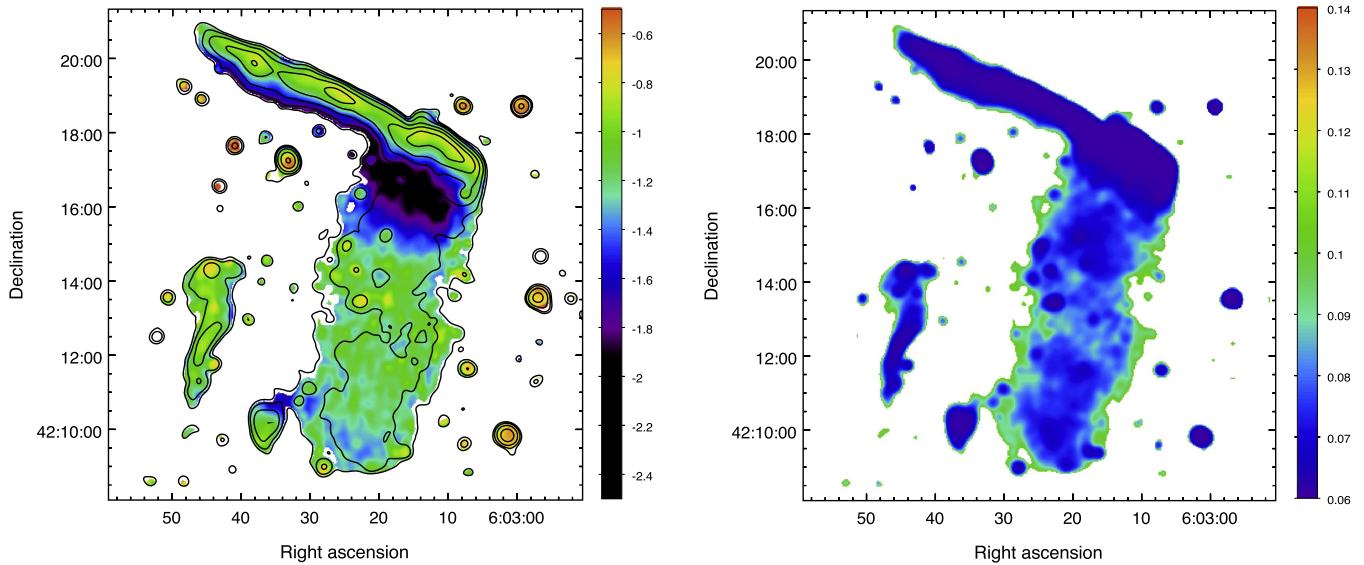


Figure 19. Left: spectral index map of the radio halo between 150 MHz and 1.5 GHz at $16''$ resolution. The image properties are given in Table 2, IM14. The contour levels are from the VLA and drawn at $[1, 2, 4, 8, \dots] \times 4.5 \sigma_{\text{rms}}$. Negative $-4.5 \sigma_{\text{rms}}$ contours are shown with dotted lines. The color bar shows spectral index α from -2.4 to -0.6 . Right: corresponding spectral index uncertainty map. The color bar shows the range of values.

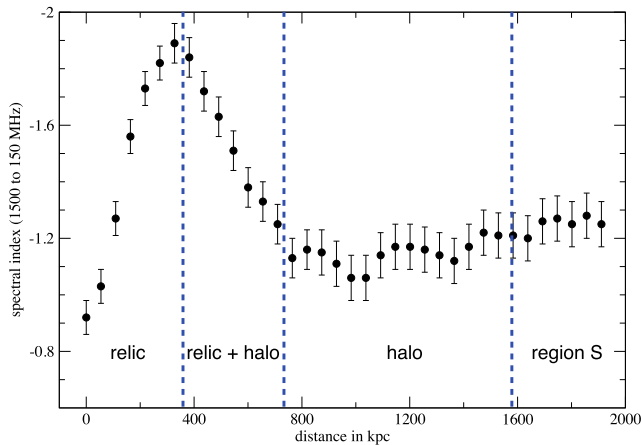


Figure 20. Extracted spectral index across relic B1 and the radio halo, from north to south. The “relic+halo” indicate combined emission from relic B and the halo. We extract spectral indices in the green regions, as indicated in Figure 7, right panel. Systematic uncertainties in the flux-scale were included in the error bars.

region S, where the spectrum steepens to -1.4 in some areas. In addition, the region S does not appear to be associated with the rest of the halo where the radio emission shows clear similarity to the X-ray emission. The total extent of region S at 1.5 GHz is about 700 kpc. This region is also characterized by a hot ICM as expected for downstream emission of the southern shock front. Considering all evidences, we suggest that the southern part of the radio halo is actually a fainter relic.

6. Summary and Conclusions

We presented deep VLA observations at 1–2 GHz of the galaxy cluster 1RXS J0603.3+4214. These observations were conducted in A, B, C, and D configurations. Thanks to the wide-band receivers, the resulting images show a very low noise level. For a restoring beam width of $1''$, a noise level of $2 \mu\text{Jy}$ is achieved. Our observations reveal the complex structure of the bright radio relic and confirm a giant radio

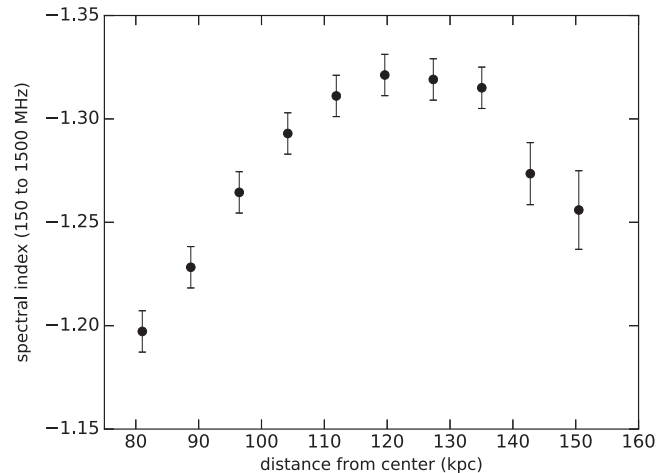


Figure 21. Spectral index distribution across the southernmost part of the radio halo (region S), with distance increasing from north to south. Regions chosen for measuring the radial radio profile are shown in Figure 7, right, with red annuli. Systematic uncertainties in the flux-scale were included in the error bars.

halo present in the cluster. Here, we summarize our primary results:

1. The Toothbrush is evidently made up of filamentary structures. The brush has a striking narrow ridge to its north with a sharp outer edge. The ridge has a width of about 25 kpc and branches to the west. We find several arc-shaped small filaments, “bristles,” in the brush region, with a width of 3–5 kpc, that are more or less perpendicular to the ridge. There are two distinct linear filaments; we label them as “double strand,” which connect the brush to B2. The B2 region also shows two thin parallel “threads,” separated by 5 kpc.
2. The spectral index map of the Toothbrush between 150 MHz and 1.5 GHz shows that at the northern edge of the ridge, the spectral index is in the range $-0.70 \leq \alpha \leq -0.80$ and steepens within the ridge. The Mach number obtained from the spectral index map is

- $\mathcal{M} = 3.3^{+0.4}_{-0.3}$. The spectral index across the double strand varies, suggesting a new injection or a change in the local magnetic field.
3. The surface brightness of the ridge downstream of the shock front at 1–2 GHz decreases by a factor of about 0.5. We suggest that the surface brightness enhancement of the ridge is caused by a projection effect.
 4. We find that the position of the ridge slightly shifts with observing frequency. This indicates that the intrinsic profile of the emission is frequency dependent, as expected for electrons cooling in the downstream region of a shock front seen edge-on.
 5. The VLA observations in combination with published GMRT and LOFAR data allowed us to compare the cooling of the electrons downstream to the shock with a model in which we adopt a significant variation of the magnetic field along the line of sight. The downstream spectral profile can be explained by a log-normal distribution of the magnetic field with a central magnetic field $B_0 \leq 5 \mu\text{G}$, log-normal width $\sigma \geq 0.5$, and a Mach number $\mathcal{M} = 3.75$. The model derived Mach number is consistent with the one obtained from the overall spectrum, namely $\mathcal{M} = 3.78^{+0.3}_{-0.2}$. The discrepancy between the X-ray and radio-derived Mach numbers may originate from the fact that the X-ray surface brightness is dominated by the densest region in the ICM along the line of sight, where the shock is rather weak.
 6. The fainter relic E comprises three bright, compact regions. These bright regions are evidently not associated with any radio galaxy, which could be the source of radio emission. We do not see a significant spectral index steepening across relic E, which would be typical for radio relics.
 7. The radio morphology of the large central region of the halo shows a close similarity to the X-ray emitting gas, confirming the connection between the hot gas and relativistic plasma. We find that the radio brightness correlates well with the X-ray brightness in the central region of the halo. The derived power-law shows a slope of $b = 1.25 \pm 0.16$, close to a linear correlation. The southernmost region of the halo appears distinct and may have a different origin.
 8. The average spectral index across the central region of the radio halo is $\alpha = -1.16 \pm 0.05$, where the uncertainty gives the raw scatter from the mean spectral index. The spectral index of the halo also shows a slight north to south gradient. The southern part of the halo is steeper and shows a spectral index gradient, suggesting a possible connection with the southern shock detected in *Chandra* observations.
 9. The sensitive and high resolution radio map allowed us to identify 32 compact radio sources within the radio halo that were not detected previously. These sources, if not subtracted in low resolution radio maps, contribute 25% of the flux measured for the halo.

K.R. and M.H. acknowledge support by the research group FOR 1254, funded by the Deutsche Forschungsgemeinschaft: “Magnetization of interstellar and intergalactic media.” Part of this work was performed at Harvard-Smithsonian Center for Astrophysics. R.J.W. is supported by a Clay Fellowship awarded by the Harvard-Smithsonian Center for Astrophysics.

Partial support for L.R. is provided by U.S. National Science Foundation grants 1211595 and 1714205 to the University of Minnesota. F.A.-S. acknowledges support from *Chandra* grant GO3-14131X. This work was performed under the auspices of the U.S. Department of Energy by Lawrence Livermore National Laboratory under Contract DE-AC52-07NA27344. We thank A. Simionescu for helping with *Chandra* X-ray analysis. M.J.J. acknowledges support for the current research from the National Research Foundation of Korea under programs 2017R1A2B2004644 and 2017R1A4A1015178.

The National Radio Astronomy Observatory is a facility of the National Science Foundation operated under cooperative agreement by Associated Universities.

This paper is based (in part) on data obtained with the International LOFAR Telescope (ILT). LOFAR (van Haarlem et al. 2013) is the Low Frequency Array designed and constructed by ASTRON. It has facilities in several countries that are owned by various parties (each with their own funding sources), and that are collectively operated by the ILT foundation under a joint scientific policy. We thank the staff of the GMRT that made these observations possible. GMRT is run by the National Centre for Radio Astrophysics of the Tata Institute of Fundamental Research. The scientific results reported in this article are based in part on observations made by the *Chandra* X-ray Observatory and published previously in van Weeren et al. (2016). Based in part on data collected at Subaru Telescope, which is operated by the National Astronomical Observatory of Japan.

ORCID iDs

K. Rajpurohit  <https://orcid.org/0000-0001-7509-2972>
W. R. Forman  <https://orcid.org/0000-0002-9478-1682>
J. H. Croston  <https://orcid.org/0000-0003-2402-9003>
F. Andrade-Santos  <https://orcid.org/0000-0002-8144-9285>
W. A. Dawson  <https://orcid.org/0000-0003-0248-6123>
H. T. Intema  <https://orcid.org/0000-0002-5880-2730>

References

- Ackermann, M., Ajello, M., Albert, A., et al. 2014, *ApJ*, **787**, 18
Ackermann, M., Ajello, M., Albert, A., et al. 2016, *ApJ*, **819**, 149
Akamatsu, H., Takizawa, M., Nakazawa, K., et al. 2012, *PASJ*, **64**, 67
Basu, K. 2012, *MNRAS*, **421**, L112
Basu, K., Vazza, F., Erler, J., & Sommer, M. 2016, *A&A*, **591**, A142
Blandford, R., & Eichler, D. 1987, *PhR*, **154**, 1
Blasi, P., & Colafrancesco, S. 1999, *Aph*, **12**, 169
Bonafede, A., Brüggen, M., van Weeren, R., et al. 2012, *MNRAS*, **426**, 40
Botteon, A., Gastaldello, F., Brunetti, G., & Kale, R. 2016, *MNRAS*, **463**, 1534
Brown, S., & Rudnick, L. 2011, *MNRAS*, **412**, 2
Brüggen, M., van Weeren, R. J., & Röttgering, H. J. A. 2012, *MNRAS*, **425**, L76
Brunetti, G., Blasi, P., Reimer, O., et al. 2012, *MNRAS*, **426**, 956
Brunetti, G., & Jones, T. W. 2014, *IMPD*, **23**, 1430007
Brunetti, G., Setti, G., Feretti, L., & Giovannini, G. 2001, *MNRAS*, **320**, 365
Brunetti, G., Zimmer, S., & Zandanel, F. 2017, *MNRAS*, **472**, 1506
Carilli, C. L., & Taylor, G. B. 2002, *ARA&A*, **40**, 319
Cassano, R., Etti, S., Brunetti, G., et al. 2013, *ApJ*, **777**, 141
Cassano, R., Etti, S., Giacintucci, S., et al. 2010, *ApJL*, **721**, L82
Cornwell, T. J., Golap, K., & Bhatnagar, S. 2008, *ISTSP*, **2**, 647
Dennison, B. 1980, *ApJL*, **239**, L93
Dolag, K., & Enßlin, T. A. 2000, *A&A*, **362**, 151
Drury, L. O. 1983, *RPPH*, **46**, 973
Eckert, D., Jauzac, M., Vazza, F., et al. 2016, *MNRAS*, **461**, 1302
Ellison, D. C., & Reynolds, S. P. 1991, *ApJ*, **382**, 242
Enßlin, T. A., Biermann, P. L., Klein, U., & Kohle, S. 1998, *A&A*, **332**, 395
Feretti, L., Brunetti, G., Giovannini, G., et al. 2004, *JKAS*, **37**, 315

- Feretti, L., Fusco-Femiano, R., Giovannini, G., & Govoni, F. 2001, *A&A*, **373**, 106
- Feretti, L., & Giovannini, G. 1996, in IAU Symp. 175, Extragalactic Radio Sources, ed. R. D. Ekers, C. Fanti, & L. Padrielli (Cambridge: Cambridge Univ. Press), 333
- Feretti, L., Giovannini, G., Govoni, F., & Murgia, M. 2012, *A&ARv*, **20**, 54
- Ferrari, C., Govoni, F., Schindler, S., Bykov, A. M., & Rephaeli, Y. 2008, *SSRv*, **134**, 93
- Finoguenov, A., Sarazin, C. L., Nakazawa, K., Wik, D. R., & Clarke, T. E. 2010, *ApJ*, **715**, 1143
- Giacintucci, S., Venturi, T., Brunetti, G., et al. 2005, *A&A*, **440**, 867
- Giacintucci, S., Venturi, T., Macario, G., et al. 2008, *A&A*, **486**, 347
- Govoni, F., Enßlin, T. A., Feretti, L., & Giovannini, G. 2001a, *A&A*, **369**, 441
- Govoni, F., & Feretti, L. 2004, *IJMPD*, **13**, 1549
- Govoni, F., Feretti, L., Giovannini, G., et al. 2001b, *A&A*, **376**, 803
- Heesen, V., Dettmar, R.-J., Krause, M., Beck, R., & Stein, Y. 2016, *MNRAS*, **458**, 332
- Hoang, D. N., Shimwell, T. W., Stroe, A., et al. 2017, *MNRAS*, **741**, 1107
- Hoeft, M., & Brüggen, M. 2007, *MNRAS*, **375**, 77
- Jaffe, W. J., & Perola, G. C. 1973, *A&A*, **26**, 423
- Jee, M. J., Dawson, W. A., Stroe, A., et al. 2016, *ApJ*, **817**, 179
- Jeltema, T. E., & Profumo, S. 2011, *ApJ*, **728**, 53
- Kang, H. 2015, *JKAS*, **48**, 9
- Kang, H., & Ryu, D. 2011, *ApJ*, **734**, 18
- Kang, H., Ryu, D., & Jones, T. W. 2012, *ApJ*, **756**, 97
- Kierdorf, M., Beck, R., Hoeft, M., et al. 2016, *A&A*, **600**, A18
- Liang, H., Hunstead, R. W., Birkinshaw, M., & Andreani, P. 2000, *ApJ*, **544**, 686
- Macario, G., Markevitch, M., Giacintucci, S., et al. 2011, *ApJ*, **728**, 82
- McMullin, J. P., Waters, B., Schiebel, D., Young, W., & Golap, K. 2007, in ASP Conf. Ser. 376, Astronomical Data Analysis Software and Systems XVI, ed. R. A. Shaw, F. Hill, & D. J. Bell (San Francisco, CA: ASP), 127
- Mohan, N., & Rafferty, D. 2015, PyBDSM: Python Blob Detection and Source Measurement, Astrophysics Source Code Library, ascl:1502.007
- Offringa, A. R., de Bruyn, A. G., Biehl, M., et al. 2010, *MNRAS*, **405**, 155
- Ogrea, G. A., Brüggen, M., van Weeren, R. J., et al. 2013, *MNRAS*, **433**, 812
- Orrú, E., Murgia, M., Feretti, L., et al. 2007, *A&A*, **467**, 943
- Owen, F. N., Rudnick, L., Eilek, J., et al. 2014, *ApJ*, **794**, 24
- Owers, M. S., Randall, S. W., Nulsen, P. E. J., et al. 2011, *ApJ*, **728**, 27
- Pearce, C. J. J., van Weeren, R. J., Andrade-Santos, F., et al. 2017, *ApJ*, **845**, 81
- Perley, R. A., & Butler, B. J. 2013, *ApJS*, **204**, 19
- Petrosian, V. 2001, *ApJ*, **557**, 560
- Pinzke, A., Oh, S. P., & Pfrommer, C. 2013, *MNRAS*, **435**, 1061
- Rau, U., & Cornwell, T. J. 2011, *A&A*, **532**, A71
- Roettiger, K., Burns, J. O., & Stone, J. M. 1999, *ApJ*, **518**, 603
- Ryu, D., Kang, H., Hallman, E., & Jones, T. W. 2003, *ApJ*, **593**, 599
- Sarazin, C. L., Finoguenov, A., & Wik, D. R. 2013, *AN*, **334**, 346
- Shimwell, T. W., Brown, S., Feain, I. J., et al. 2014, *MNRAS*, **440**, 2901
- Shimwell, T. W., Markevitch, M., Brown, S., et al. 2015, *MNRAS*, **449**, 1486
- Skillman, S. W., Xu, H., Hallman, E. J., et al. 2013, *ApJ*, **765**, 21
- Stroe, A., Shimwell, T., Rumsey, C., et al. 2016, *MNRAS*, **455**, 2402
- Stroe, A., van Weeren, R. J., Intema, H. T., et al. 2013, *A&A*, **555**, A110
- Trasatti, M., Akamatsu, H., Lovisari, L., et al. 2015, *A&A*, **575**, A45
- Uchida, Y., Simionescu, A., Takahashi, T., et al. 2016, *PASJ*, **68**, S20
- Vacca, V., Feretti, L., Giovannini, G., et al. 2014, *A&A*, **561**, A52
- van Haarlem, M. P., Wise, M. W., Gunst, A. W., et al. 2013, *A&A*, **556**, A2
- van Weeren, R. J., Andrade-Santos, F., Dawson, W. A., et al. 2017a, *NatAs*, **1**, 0005
- van Weeren, R. J., Brüggen, M., Röttgering, H. J. A., et al. 2011, *A&A*, **533**, A35
- van Weeren, R. J., Brunetti, G., Brüggen, M., et al. 2016, *ApJ*, **818**, 204
- van Weeren, R. J., Ogrea, G. A., Jones, C., et al. 2017b, *ApJ*, **835**, 197
- van Weeren, R. J., Röttgering, H. J. A., Brüggen, M., & Hoeft, M. 2010, *Sci*, **330**, 347
- van Weeren, R. J., Röttgering, H. J. A., Intema, H. T., et al. 2012a, *A&A*, **546**, A124
- van Weeren, R. J., Röttgering, H. J. A., Rafferty, D. A., et al. 2012b, *A&A*, **543**, A43
- Vazza, F., Roediger, E., & Brüggen, M. 2012, *A&A*, **544**, A103
- Venturi, T., Giacintucci, S., Dallacasa, D., et al. 2013, *A&A*, **551**, A24